GRB 070125 and the environments of spectral-line poor afterglow absorbers[★]

A. De Cia,[1]† R. L. C. Starling,[2] K. Wiersema,[2] A. J. van der Horst,[3] P. M. Vreeswijk,[1] G. Björnsson,[1] A. de Ugarte Postigo,[4] P. Jakobsson,[1] A. J. Levan,[5] E. Rol,[6] S. Schulze[1] and N. R. Tanvir[2]

[1]*Centre for Astrophysics and Cosmology, Science Institute, University of Iceland, Dunhaga 5, IS-107 Reykjavik, Iceland*
[2]*Department of Physics and Astronomy, University of Leicester, University Road, Leicester LE1 7RH*
[3]*Universities Space Research Association, NSSTC, 320 Sparkman Drive, Huntsville, AL 35805, USA*
[4]*Dark Cosmology Centre, Niels Bohr Institute, University of Copenhagen, 2100 Copenhagen Ø, Denmark*
[5]*Department of Physics, University of Warwick, Coventry CV4 7AL*
[6]*Astronomical Institute, University of Amsterdam, Science Park 904, 1098 XH Amsterdam, the Netherlands*

ABSTRACT

GRB 070125 is among the most energetic bursts detected and the most extensively observed so far. Nevertheless, unresolved issues are still open in the literature on the physics of the afterglow and on the gamma-ray burst (GRB) environment. In particular, GRB 070125 was claimed to have exploded in a galactic halo environment, based on the uniqueness of the optical spectrum and the non-detection of an underlying host galaxy. In this work we collect all publicly available data and address these issues by modelling the near-infrared to X-ray spectral energy distribution (SED) and studying the high signal-to-noise ratio Very Large Telescope/FOcal Reducer/low dispersion Spectrograph afterglow spectrum in comparison with a larger sample of GRB absorbers. The SED reveals a synchrotron cooling break in the ultraviolet, low equivalent hydrogen column density and little reddening caused by a Large Magellanic Cloud type or Small Magellanic Cloud type extinction curve. From the weak Mg II absorption at $z = 1.5477$ in the spectrum, we derived $\log N(\text{Mg\,II}) = 12.96^{+0.13}_{-0.18}$ and upper limits on the ionic column density of several metals. These suggest that the GRB absorber is most likely a Lyman limit system with a $0.03 < Z < 1.3\,Z_\odot$ metallicity. The comparison with other GRB absorbers places GRB 070125 at the low end of the absorption-line equivalent width distribution, confirming that weak spectral features and spectral-line poor absorbers are not so uncommon in afterglow spectra. Moreover, we show that the effect of photoionization on the gas surrounding the GRB, combined with a low $N(\text{H\,I})$ along a short segment of the line of sight within the host galaxy, can explain the lack of spectral features in GRB 070125. Finally, the non-detection of an underlying galaxy is consistent with a faint GRB host galaxy, well within the GRB host brightness distribution. Thus, the possibility that GRB 070125 is simply located in the outskirts of a gas-rich, massive star-forming region inside its small and faint host galaxy seems more likely than a gas-poor, halo environment origin.

Key words: gamma-ray burst: individual: GRB 070125.

1 INTRODUCTION

The progenitors of long gamma-ray bursts (GRBs) are believed to be rapidly rotating massive stars (for a review, see Woosley 1993 and MacFadyen & Woosley 1999). The observations of some supernovae (SNe) associated with GRBs have corroborated this hypothesis (Woosley & Bloom 2006; Hjorth & Bloom 2011, and references therein), implying that long GRBs are located in star-forming regions. Within the fireball model (see Piran 2004 and Mészáros 2006, for a review) the GRB afterglow is produced by the interaction of

an expanding blast wave with the surrounding medium. The external shocks are responsible for the synchrotron radiation, from X-rays to optical and down to radio frequencies as the blast wave decelerates. The spectral energy distribution (SED) and its evolution are described by the fireball model (Sari, Piran & Narayan 1998; Granot & Sari 2002). Modelling the SED can simultaneously provide information on the intrinsic spectral shape of the GRB, i.e. the fireball physical parameters, and on the GRB local and host galaxy environment. In the latter case, this includes the circumburst density or the line-of-sight dust extinction, depending on whether the broad-band blast wave, down to radio frequencies, (e.g. Panaitescu & Kumar 2002; Björnsson, Gudmundsson & Jóhannesson 2004; de Ugarte Postigo et al. 2005; van der Horst et al. 2005; Jóhannesson, Björnsson & Gudmundsson 2006; Rol et al. 2007) or the optical-to-X-ray SED is modelled (Starling et al. 2007, 2008; Schady et al. 2010; Zafar et al. 2011). The interstellar medium (ISM) of the GRB host galaxy can also be investigated through absorption-line spectroscopy of the afterglow, providing the chemical composition of different ions in the absorbing gas and possibly its metallicity (e.g. Vreeswijk et al. 2004; Fynbo et al. 2006; Savaglio 2006; Prochaska et al. 2007; Ledoux et al. 2009).

GRB 070125 is among the most energetic bursts detected so far, both in the prompt high energy release (with an isotropic emitted energy $E_{iso} \sim 10^{54}$ erg; Bellm et al. 2008) and its afterglow (with a collimation-corrected blast wave kinetic energy of more than 10^{52} erg; Chandra et al. 2008). The optical afterglow is amongst the brightest at around one day after the burst, when redshift-corrected ($R_c \sim 17$ shifted at $z = 1$; Updike et al. 2008; Kann et al. 2010). The brightness of the event allowed a global monitoring campaign of the afterglow, resulting in one of the largest data sets collected so far, covering radio, mm, near-infrared (NIR), optical, ultraviolet (UV) and X-rays (Cenko et al. 2008; Chandra et al. 2008; Dai et al. 2008; Updike et al. 2008; Kann et al. 2010). Despite the observational effort, there is still much debate over both the jet properties and the type of environment in which GRB 070125 was situated.

Based on the absence of strong spectral features and a bright underlying host, GRB 070125 was reported to be the first long GRB to have exploded in a galactic halo environment. This would pose a challenge to modelling of progenitor objects. In particular, the GRB site was suggested to be in a compact stellar cluster that resulted from the interaction of two blue faint galaxies at a projected distance of ≈ 27 and ≈ 46 kpc[1] (Cenko et al. 2008). However, a very limited sample of GRB afterglows was used as reference to argue the peculiarity of the spectrum [few spectral features, weak Mg II absorption and low inferred $N(\text{H I})$]. By contrast, from a partial broad-band SED analysis, Chandra et al. (2008) found a very high circumburst density ($n \approx 50$ cm^{-3}, from the kinetic energy, and $n \approx 40$ cm^{-3}, from the broad-band modelling of the SED). However, in their data it was not possible to distinguish between a constant and a wind-like density profile, nor to firmly constrain the putative (chromatic) jet break and the inverse Compton influence on it. On the other hand, Dai et al. (2008) claimed a 'textbook' achromatic jet break at 5.8 d after the burst. Another open issue is the presence or absence of a synchrotron cooling break in the SED between the optical and X-rays and the agreement or not of the data with the fireball closure, as discussed in (Updike et al. 2008).

In this work, we collect the multitude of observations spread through the literature and analyse them together in order to obtain a coherent picture of the GRB environment. In particular, we investigate the location of a synchrotron cooling break and the environment dust and metal content by studying the NIR-to-X-ray SED at different epochs. Furthermore, we analyse the very high signal-to-noise ratio (S/N) Very Large Telescope/FOcal Reducer/low dispersion Spectrograph (VLT/FORS) spectrum of the afterglow and discuss the possible implications for the absorber environment. We then compare the spectral features to the large sample of GRB afterglows with redshift collected in Fynbo et al. (2009) and two subsamples of GRBs potentially similar to GRB 070125. The observations and data analysis are presented in Sections 2 and 3, respectively, the SED modelling in Section 4 and the discussion in Section 5. Our conclusions are summarized in Section 6.

Throughout the paper we use the convention $F_\nu(t) \propto t^{-\alpha} \nu^{-\beta}$ for the flux density of the afterglow, where α is the temporal slope and β is the spectral slope. We refer to the solar abundances measured by Asplund et al. (2009) and adopt cm^{-2} as the linear unit of column densities, N. Hereafter, we assume a standard Λ cold dark matter cosmology with $H_0 = 70.4$ km s^{-1} Mpc^{-1}, $\Omega_M = 0.27$ and $\Omega_\Lambda = 0.73$ (Jarosik et al. 2011).

2 OBSERVATIONS AND DATA REDUCTION

GRB 070125 was localized by the Interplanetary Network (*Mars Odyssey*, *Suzaku*, *INTEGRAL* and *RHESSI*) at $t_0 = 07{:}20{:}45$ UT (Hurley et al. 2007), and subsequently observed by *Swift*. The high-energy properties of the GRB prompt emission are discussed in Bellm et al. (2008). The optical afterglow was first localized by Cenko & Fox (2007) at the position RA $= 07^h 51^m 17{.}^s 75$ and Dec. $= +31°09'04{.}''2$ (J2000), and the host galaxy redshift, $z = 1.547$, was determined from an Mg II doublet absorption in a Gemini-North/Gemini Multi-Object Spectrograph (GMOS) afterglow spectrum (Fox et al. 2007). Thanks to the brightness of the afterglow, a multitude of observations in the optical and NIR could be secured with 20 telescopes (e.g. Chandra et al. 2008; Updike et al. 2008; Kann et al. 2010).

2.1 *Swift* XRT

The *Swift* X-ray telescope (XRT; Burrows et al. 2005) began observing the GRB 070125 field 12.97 h after the trigger and continued to monitor the decaying afterglow in photon counting mode for 15 orbits or 173 ks of exposure time. The last observations ended on 2007 February 12 at 23:50 UT, 18.69 d after the burst trigger. We obtained the XRT event files from the UK *Swift* Science Data Centre archive[2] and processed them using the standard *Swift* XRT pipeline software version 0.12.3 and calibration data base CALDB-11.

We extracted X-ray spectra and response files for each orbit individually as well as a late-time combined spectrum comprising orbit 3 onwards. Spectra were grouped such that a minimum of 20 counts fell in each bin, and spectral analysis was performed with the XSPEC spectral fitting package (Arnaud 1996), version 12.6.0.

We extracted a 0.3–10 keV light curve and transformed the count rate to flux using three conversion factors derived from spectra of orbits 1, 2 and 3 onwards of 1 count s$^{-1} = 4.44$, 4.09 and 3.67×10^{-11} erg cm^{-2} s^{-1}, respectively. These three intervals were selected in order to apply the proper conversion factor to each regime, from the brighter to the late fainter epochs. We also collected the dynamically binned XRT flux light curve from the *Swift* repository (Evans et al. 2007), which was converted from count rate to flux with the

---

[1] Derived from the 3.2 and 5.5 arcsec angular distance between the afterglow and the two putative host galaxies.

[2] http://www.swift.ac.uk/swift_portal
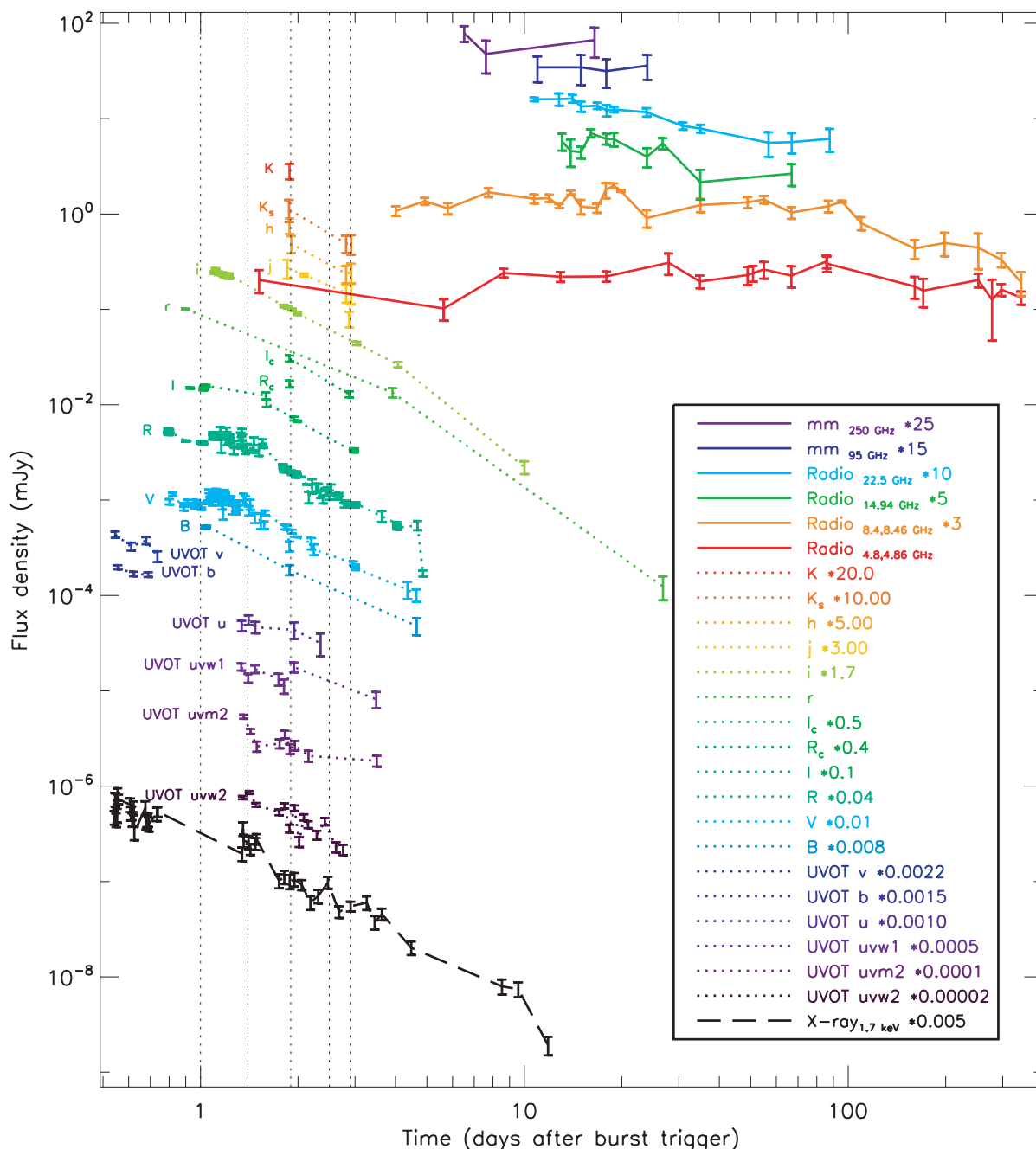
Figure 1. The radio to X-ray afterglow light curves, scaled with the factors reported in the legend for a clearer display. The dashed vertical lines mark the SED times.

average conversion factor, 1 count s^{-1} = 3.8×10^{-11} erg cm^{-2} s^{-1}. We then converted the binned and unbinned light curves into flux density F_ν at 1.73 keV, the logarithmic average of the XRT band (0.3–10 keV), assuming a spectral slope $\beta = 1.1$, as found in Section 3.1. The binned XRT light curve is shown in Fig. 1.

2.2 *Swift* UVOT

The afterglow of GRB 070125 was detected with the *Swift* ultraviolet/optical telescope (UVOT; Roming et al. 2005) in all six lenticular filters spanning from *v* to *uvw2* (covering a range between 546 and 193 nm). These observations were coincident with those of the *Swift* XRT during the period from 12.97 h to 18.69 d after the trigger. The

optical/UV transient was detected out to 3.5 d after the trigger. We inspected the UVOT sky images and selected those of sufficient quality to perform photometry to an accuracy of 0.4 mag or better. We performed photometry on the images using the UVOTSOURCE task included in HEASOFT v6.7 and calibrations provided by Poole et al. (2008). We used a 5-arcsec radius source extraction region, and a nearby 20-arcsec radius source-free background region. The UVOT photometry is reported in Appendix A.

2.3 VLT/FORS2

Starting at 04:25 UT on 2007 January 26 (21.1 h post-burst), a series of spectra were obtained with VLT/FORS2 in long-slit spectroscopy

Table 1. VLT/FORS2 observation log on date 2007 January 26.

Start time UT (hh:mm:ss)	Δt^a (h)	Exp. time (min)	Grism	Coverage λ (Å)	Resolution FWHM (Å)	Airmass	Seeing (arcsec)	S/N per pixel (mean)
04:25:24	21.20	15	300V	3190–9640	10.7	1.8	0.80	54
04:53:31	21.80	30	600z	7460–10740	5.3	1.8	0.72	39
05:25:14	22.32	30	1400V	4630–5930	2.0	1.9	0.87	39
05:56:40	22.85	30	1200R	5870–7370	2.2	2.1	0.62	43

^{a}Mid-exposure time after the burst trigger (07:20:45 UT).

mode with a 1.0−arcsec wide slit. The sequence of grisms used was 300V, 600z+OG590, 1400V and 1200R+GG435. This allowed us to both cover a larger wavelength window with the lower resolution grism (300V) and obtain mid-resolution spectroscopy for different regions of the spectrum. Cosmic ray removal was performed on each individual spectrum using the Laplacian Cosmic Ray Identification algorithm of van Dokkum (2001). The seeing remained relatively stable during the observations, between 0.6 and 0.9 arcsec, yielding the spectral resolutions and excellent S/N, reported in Table 1.

2.4 Literature data collection

We gathered all the data on GRB 070125 available in the literature from Chandra et al. (2008), Updike et al. (2008) and Kann et al. (2010), covering radio to optical frequencies. We exclude the observations from GRB Coordinates Network (GCNs) circulars reported in Chandra et al. (2008), with the exception of three NIR data points[3] (K_s, J, H), given the limited NIR coverage. In addition, we include the *Swift* UVOT and XRT observations that we analysed. In all, 365 NIR to UV photometric data points, for a total of 19 filters, and 77 radio and mm data points were collected. We converted the magnitudes into flux density using the zero-points available for each specific filter. All the magnitudes were corrected for Galactic extinction [$E(B-V) = 0.052$ mag], as listed by Schlegel, Finkbeiner & Davis (1998), and for transmission through the Lyα forest at redshift 1.5477 in each optical and UV band (e.g. Madau 1995) adopting the spectral slope, $\beta = 0.58$, as derived from the optical SED (Updike et al. 2008). The corresponding transmissions are $tr_U = 0.996$, $tr_{uvw1} = 0.848$, $tr_{uvm2} = 0.633$ and $tr_{uvw2} = 0.539$. The light curves for each filter are shown in Fig. 1. The data set that we used is rather inhomogeneous, as it is collected from different sources in the literature. Despite the uncertainty on the single data points, the interpolations of the flux densities at a given epoch are weighted by these errors, giving more importance to the more precise measurements. Thus, the uncertainties due to the inhomogeneous sample are limited, given the large data set, and cannot significantly influence our results.

3 SPECTRAL ANALYSIS

3.1 X-ray spectrum

We first independently modelled the spectrum of each orbit with a simple power law, absorbed by gas at redshift $z = 1.5477$, as derived

[3] The three GCN measurements do not strongly influence the NIR light curves, since they are very close to the NIR photometry reported by Updike et al. (2008) at 2.9 after the burst. After acceptance of this paper, it was brought to our attention that the NIR data points obtained by PAIRITEL which we gathered from GCN 6054 in Chandra et al. (2008) and Updike et al. (2008) are in fact the same data set, but with slightly different reported mid-times. This duplication has no effects on the results and conclusions we presented in our paper.

from the spectral analysis (see Section 3.2), finding no evidence for spectral variability in the XRT data alone within this model. The Galactic absorption was fixed at 4.3×10^{20} cm^{-2} (Kalberla et al. 2005). We then extracted the time-averaged spectrum over the whole XRT observation. Modelling the overall spectrum, we derived a power-law spectral slope $\beta = 1.06^{+0.09}_{-0.13}$, a soft X-ray absorption at the host galaxy redshift, $N(\mathrm{H}) = 15.5^{+13.9}_{-14.9} \times 10^{20}$ cm^{-2} and $\chi^2_\nu = 0.7$ for 40 degrees of freedom (d.o.f.). The quoted errors correspond to 90 per cent confidence. The modelled absorbed flux (0.3–10 keV) is $F = 1.83 \times 10^{-13}$ erg cm^{-2} s^{-1}. The uncertainty on the host $N(\mathrm{H})$ is sufficiently large that it would be consistent with only Galactic foreground absorption. Given that the Galactic $N(\mathrm{H})$ is typically $10^{20} \lesssim N(\mathrm{H}) \lesssim 10^{21}$ cm^{-2} (with uncertainties of about ∼10 per cent; Dickey & Lockman 1990; Kalberla et al. 2005), it is often not possible to tightly constrain a low GRB host galaxy $N(\mathrm{H})$.

3.2 Optical spectrum

The absorption lines detected in the FORS spectra are listed in Table 2, along with the equivalent widths (EWs). The absorption lines associated with the $z = 1.5477$ system are shown in Fig. 2. The apertures used to measure the EWs are derived from the resolution in each grism, i.e. twice the full width at half-maximum (FWHM) of the arc lines ($2 \times$ FWHM$_\mathrm{arc}$), justified by the narrowness of both the Mg II and C IV lines. These lines are unresolved, the width of the Mg II $\lambda 2803$ Å line being FWHM$_{2803} \sim 70$ km s^{-1}.

The low spectral resolution does not allow us to directly derive the column density from the detected EW in the optically thin limit, even for the weak EWs we measure, since the lines may be saturated. In particular, this could affect the Mg II, despite the EW$_{2796}$/EW$_{2803} \sim 2$ ratio of the Mg II $\lambda 2796$ to Mg II $\lambda 2803$ Å suggests little or no saturation. A proper curve of growth (CoG; e.g. Mihalas 1978) analysis would require many transitions to constrain the b value (Doppler parameter, $b = \sqrt{2} \times \sigma_\mathrm{Gaussian}$). However, we can benefit from the excellent S/N and the narrowness of the transitions to constrain the column density with the CoG, despite the limited number of detections. We studied the CoG evolution with the

Table 2. Detected absorption lines in the VLT/FORS spectra.

Ion	λ_rest (Å)	λ_obs (Å)	z	EW$_\mathrm{rest}^a$ (Å)	σ^b
		300V			
C IV	1549	3949.55	1.5497	0.77 ± 0.09	8.5
		1200R			
Mg II	2796.35	7124.30	1.5477	0.29 ± 0.04	7.2
Mg II	2803.53	7142.74	1.5478	0.14 ± 0.02	7.0
		1400V			
Na I	5891.58	5891.58	0.000	0.68 ± 0.08	8.5
Na I	5897.56	5897.56	0.000	0.41 ± 0.08	5.1

^{a}1σ errors; ^{b}significance.
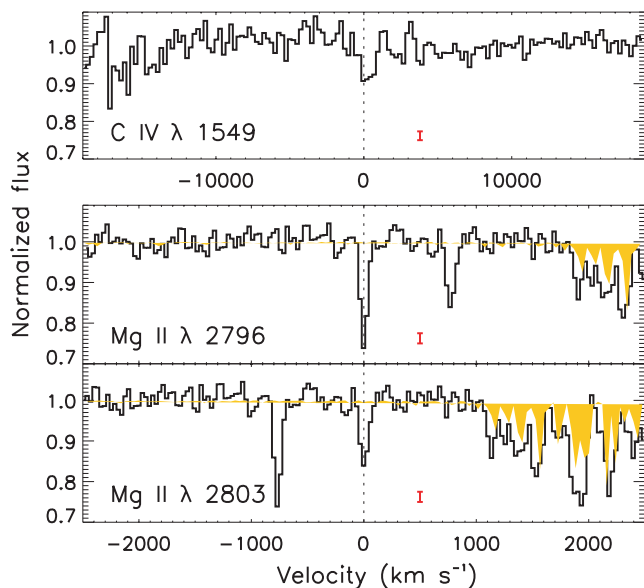
Figure 2. Absorption lines detected in the FORS spectra at host galaxy redshift $z = 1.5477$. Note that the C IV spectrum, observed with the lowest resolution, spans a larger velocity range (top panel). The error bars show the mean error spectrum, averaged within $\pm 2000\,\mathrm{km\,s^{-1}}$ from the line position. The telluric features are highlighted.

b value of the Mg II $\lambda\lambda 2796$, 2803 transitions. The rest-frame EW of the absorption lines falls between the linear and the saturated part of the CoG, i.e. the Mg II column density has a slight dependency on the b value. We can limit the plausible range to $10 < b < 44\,\mathrm{km\,s^{-1}}$, as the line broadening must be narrower than the observed FWHM $\sim 70\,\mathrm{km\,s^{-1}}$ (FWHM $= 2\sqrt{2\ln 2}\,b/\sqrt{2} = 1.665\,b$). The lower limit is selected from the lowest velocity width of low-ionization line profiles observed in Ultraviolet and Visual Echelle Spectrograph (UVES) quasi-stellar object absorbers[4] (Ledoux et al. 2006). The $\lambda 2803$ absorption line gives the tightest constraint, $\log N(\mathrm{Mg\,II}) = 12.96^{+0.13}_{-0.18}$ (1σ errors), derived considering the median column density within the b and 1σ EW interval. The Mg II $\lambda 2803$ CoG is shown in Fig. 3. So far we used EW_{2803} and the limits on b to derive the Mg II column density. On the other hand, the Mg II column density derived from the $\lambda 2803$ allows us to use the $\lambda 2796$ CoG to further constrain the b value to be $30 < b < 44\,\mathrm{km\,s^{-1}}$. With these limits on b, we cannot derive the C IV column density, because the $\lambda 1549$ CoG shows that the absorption line is saturated. We list the 3σ upper limits on the non-detected lines in Table 3, measuring the noise level at each line position, again with $2 \times \mathrm{FWHM_{arc}}$ apertures. The excellent S/N allows us to put strict constraints on the column densities of some ions, such as Fe II.

[4] The lower observed value is $\Delta v = 17\,\mathrm{km\,s^{-1}}$, where Δv is the velocity width that covers 95 per cent of the complex line profile. If the line profile is a single Gaussian, then $\Delta v = 1.96\,\sigma_{\mathrm{Gaussian}} = 1.39\,b$, corresponding to a minimum observed $b = 12\,\mathrm{km\,s^{-1}}$. This represents only an estimate of the width of the observed line profile, despite the single components of the complex profile not being resolved with low-resolution spectroscopy. The UVES spectrum of GRB 050730 showed single component line profiles with $b = 10\,\mathrm{km\,s^{-1}}$. Of course, the possibility that the line profile is a single component with a very low b can never be totally excluded. This would result in higher saturation of such component, leading to a higher value of $N(\mathrm{Mg\,II})$. A higher $N(\mathrm{Mg\,II})$ would only strengthen the conclusions of this paper. The Mg II column density derived in the optically thin limit is $\log N(\mathrm{Mg\,II}) = 12.88^{+0.06}_{-0.07}$.
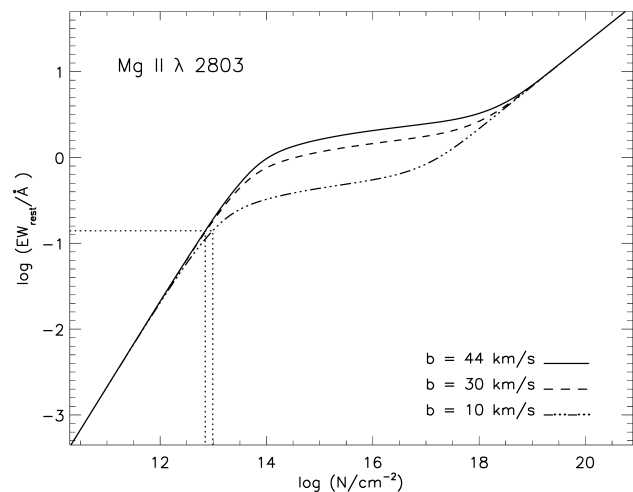
Figure 3. CoG for Mg II $\lambda 2803$ for different b values. The dotted lines correspond to the measured $\mathrm{EW_{rest}}$. Including the 1σ errors on the EW, we derive $\log N(\mathrm{Mg\,II}) = 12.96^{+0.13}_{-0.18}$.

Table 3. 3σ line detection limits with corresponding column densities computed in the optically thin limit.

Ion	λ_{rest} (Å)	$\mathrm{EW_{rest}}$ (Å)	$\log N$	Grism
C II	1334.53	<2.85	<15.15	300V
Si IV	1393.75	<1.91	<14.32	300V
Si II	1526.71	<0.44	<14.23	300V
Al II	1670.79	<0.29	<12.80	300V
Ni II	1741.55	<0.27	<14.37	300V
S I	1807.31	<0.25	<13.89	300V
Al III	1854.72	<0.09	<12.76	1400V
Ti II	1910.93	<0.07	<13.36	1400V
Zn II	2026.14	<0.06	<12.55	1400V
Cr II	2056.25	<0.07	<13.23	1400V
Fe II	2382.76	<0.07	<12.61	1200R
Fe II*	2396.35	<0.07	<12.64	1200R

*First fine-structure energy level.

We identified Galactic ($z = 0$) absorption of the Na I $\lambda\lambda 5891$, 5897 doublet in both 1200R and 1400V FORS spectra, and we report the EW in Table 2. The Galactic absorption is shown in Fig. A1. The Galactic reddening in the direction of the target measured by Schlegel et al. (1998) is $E(B - V) = 0.052 \pm 0.008$ mag. For comparison, we derive the reddening from the Galactic Na I – $E(B - V)$ correlation given by Munari & Zwitter (1997), finding a higher reddening value, $E(B - V) \sim 0.20$ mag, but consistent within the reddening uncertainty in their correlation (0.15 mag).

4 AFTERGLOW MODELLING: THE NIR-TO-X-RAY SED

In order to investigate any temporal evolution of the SED from the NIR to X-ray frequencies, we evaluated the SED at five epochs after the burst trigger. The SED times 1.0, 1.4, 1.9, 2.5 and 2.9 d were selected in order to maximize the NIR to UV data coverage for each epoch and minimize extrapolations, as shown in Fig. 1. For each SED epoch, we combine the available NIR to UV photometric data points and the ones derived by interpolating or extrapolating the light curves where necessary, for each filter. The flux interpolations at particular times were performed locally, i.e. using up to three adjacent data points on each side. The X-ray

spectra at the five epochs were produced by scaling the overall X-ray spectrum to the actual count rate at each time of interest. This choice allowed us to preserve the best S/N, justified by the lack of spectral evolution measured for the X-ray data alone (see Section 3.1).

The SED was created and fitted in count space using the ISIS spectral fitting package (Houck & Denicola 2000) and following the method given by Starling et al. (2007), having the advantage that no model for the X-ray data needed to be assumed a priori. Furthermore, as all the data are flux-calibrated, no additional offset was needed. We fit the SED using models consisting of an absorbed power law or absorbed broken power law with slopes free or fixed to a slope difference of $\Delta\beta = 0.5$, as expected for a cooling break (Sari et al. 1998). The latter model is referred to as 'tied broken power law', since the spectral slope at lower energies than the break energy E_{bk}, β_1, is tied to the spectral slope at higher energies, β_2 ($\beta_1 = \beta_2 - 0.5$). The intrinsic optical extinction was modelled with either Milky Way (MW), Large Magellanic Cloud (LMC) or Small Magellanic Cloud (SMC) extinction curves, as parametrized by Pei (1992). The X-ray absorption is modelled with the XSPEC model *zphabs*, assuming solar metallicity. We also tested the model for a lower metallicity. The results for each independent epoch are presented in Appendix A (Table A2). We note that the flaring activity, also reported by Updike et al. (2008), significantly affects the SED modelling at early epochs.

We also explored the SED evolution by tying some parameters between the epochs, where they are not expected to change in time. The tied parameters are the host $E(B - V)$ and $N(H)$, since we do not expect the host extinction and absorption to vary at two days after the burst, and the spectral slope at higher energies, β_2, since we detected no significant X-ray spectral evolution (Section 3.1). The spectral slope at lower energies, β_1, and E_{bk} were left free to vary between the epochs. We excluded epochs I and II from the SED fit tied between the epochs to avoid the flaring activity at early times (see Fig. 1). These joint fits are listed in Table 4, and Fig. 4 shows the best-fitting joint model to the last three epochs. We discuss the best-fitting model and a comparison with the results of broad-band SED modelling in Section 5.

Table 4. NIR-to-X-ray SED modelling with a single power law (PL), a broken power law (BPL) and a tied broken power law (TIED BPL), where the spectral slopes are tied to differ by $\Delta\beta \equiv 0.5$, as expected for a synchrotron cooling break (Sari et al. 1998). Each model is jointly fitted to the SED at epochs III, IV and V (1.9, 2.5 and 2.9 d after the trigger) by tying some parameters between the epochs, i.e. $E(B - V)$, $N(H)$ and β_2 are allowed to vary but not between the epochs. The best-fitting model (underlined) is a broken power law with $\beta_2 = 1.18 \pm 0.01$ and a break energy $E_{bk} = 7.6^{+4.0}_{-1.8}, 5.3^{+1.2}_{-1.0}, 4.3^{+0.9}_{-0.6}$ eV, in the UV. The $N(H)$ is consistent with the Galactic value, while a low dust content $E(B - V) = 0.016 \pm 0.007$ mag can be derived from the SED, equally well described by SMC and LMC extinction curves. The errors refer to a 90 per cent confidence limit, and are solely statistical error, i.e. they do not include systematic errors.

Ext. type	Model	χ^2_ν [d.o.f.]	$E(B-V)$ (mag)	$N(H)$ (10^{22} cm^{-2})	β_1	β_2	E_{bk} (eV)	Epoch
	PL	4.06 [148]	<0.0018	<1.3 × 10⁻⁶	1.083 ± 0.008	–	–	III
					1.091 ± 0.009	–	–	IV
					$1.069^{+0.010}_{-0.009}$	–	–	V
	BPL	2.85 [146]	0.015 ± 0.007	<1.2 × 10⁻⁶	0.828 ± 0.065	1.18 ± 0.01	$7.5^{+3.7}_{-1.8}$	III
SMC					$0.72^{+0.08}_{-0.09}$		$5.4^{+1.3}_{-0.9}$	IV
					$0.48^{+0.12}_{-0.13}$		$4.5^{+0.9}_{-0.7}$	V
	TIED BPL	2.96 [147]	0.017 ± 0.006	<1.2 × 10⁻⁶	$\beta_2 - 0.5$	1.18 ± 0.01	$5.1^{+0.9}_{-0.7}$	III
							$5.1^{+0.8}_{-0.7}$	IV
							$6.0^{+1.1}_{-0.8}$	V
	PL	4.06 [148]	<0.0018	<1.3 × 10⁻⁶	1.083 ± 0.008	–	–	III
					1.091 ± 0.009	–	–	IV
					$1.069^{+0.010}_{-0.009}$	–	–	V
	BPL	2.84 [146]	0.016 ± 0.007	<1.3 × 10⁻⁶	$0.835^{+0.065}_{-0.063}$	1.18 ± 0.01	$7.6^{+4.0}_{-1.8}$	III
LMC					$0.72^{+0.08}_{-0.09}$		$5.3^{+1.2}_{-1.0}$	IV
					$0.45^{+0.12}_{-0.13}$		$4.3^{+0.9}_{-0.6}$	V
	TIED BPL	2.97 [147]	0.016 ± 0.006	<1.2 × 10⁻⁶	$\beta_2 - 0.5$	1.18 ± 0.01	$5.2^{+0.9}_{-0.7}$	III
							$5.1^{+0.8}_{-0.7}$	IV
							$6.0^{+1.2}_{-0.8}$	V
	PL	4.06 [148]	<0.0017	<1.3 × 10⁻⁶	1.083 ± 0.008	–	–	III
					1.091 ± 0.009	–	–	IV
					$1.069^{+0.010}_{-0.009}$	–	–	V
	BPL	2.99 [146]	0.008 ± 0.007	<1.2 × 10⁻⁶	$1.089^{+0.010}_{-0.009}$	1.184 ± 0.016		III
MW					$0.71^{+0.07}_{-0.08}$		$6.1^{+1.7}_{-1.0}$	IV
					$0.50^{+0.10}_{-0.12}$		<5	V
	TIED BPL	4.14 [147]	<0.0016	<1.2 × 10⁻⁶	$\beta_2 - 0.5$	$1.581^{+0.006}_{-0.005}$	$10.00^{+0.00}_{-6.56} \times 10^3$	III
							$3.17^{+6.83}_{-0.77} \times 10^3$	IV
							$7.58^{+2.42}_{-4.30} \times 10^3$	V
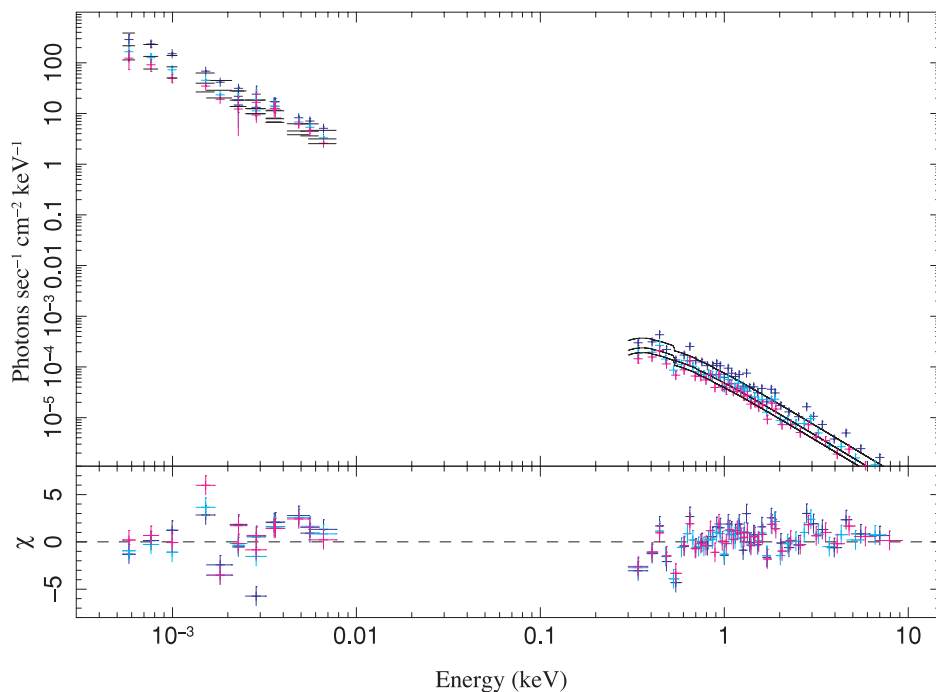
Figure 4. Broken power-law fit to the epoch III (blue), IV (cyan) and V (magenta) NIR-to-X-ray SED, with LMC dust extinction and tied parameters between the epochs.

5 DISCUSSION

5.1 The spectral energy distribution

The jointly fitted epoch III–V NIR-to-X-ray SED of GRB 070125 is best described by a broken power law with $\beta_2 = 1.18 \pm 0.01$ (tied between the epochs), and $\beta_1 = 0.835^{+0.065}_{-0.063}, 0.72^{+0.08}_{-0.09}$ and $0.45^{+0.12}_{-0.13}$ for epoch III, IV and V, respectively ($\chi^2_\nu = 2.84$ for 146 d.o.f., see Table 4). The break energy, $E_{\rm bk}$, is located in the UV, and there is a marginal hint for its evolution[5] in time towards longer wavelengths: $\lambda_{\rm bk} = 1632^{+506}_{-562}, 2340^{+544}_{-432}$ and 2885^{+468}_{-499} Å from epochs III, IV and V. The quoted errors refer to 90 per cent confidence. The spectral slope differences suggest that the spectral break is a synchrotron cooling break, and a fit with a tied broken power law ($\Delta\beta = 0.5$) provides an adequate fit indeed ($\chi^2_\nu = 2.97$ for 147 d.o.f.) and the same $\beta_2 = 1.18 \pm 0.01$. The free broken power law is slightly preferred with respect to the tied broken power law, but the latter cannot formally be excluded (F-test null probability of 0.62). Regardless of the extinction model used, a broken power law always gives a significantly better fit than a single power law from the NIR to X-ray regime. The F-test probability of the broken power law over the power-law fit improvement being obtained by chance is between 10^{-12} and 7×10^{-11} with all extinction laws in the epochs III–V joint fits, confirming the significance of the improvement.

The dust extinction $A_V = 0.05 \pm 0.02$ mag [for $R_V = A_V/E(B - V) = 3.16$ in the LMC; Pei 1992] is best modelled with an LMC or SMC extinction curve, suggesting a low-metallicity GRB absorber.[6]

---

[5] Consistent with a time evolution of the synchrotron cooling frequency as $\nu_c \propto t^{-1/2}$ expected for a blast wave expanding in a constant ISM in the slow cooling regime ($\nu_m < \nu_c$; e.g. Sari et al. 1998). However, the evolution is not significant, since fitting a constant to the three $E_{\rm bk}$ values provides $\chi^2 = 1.4$ (for 2 d.o.f.).

[6] [Fe/H] $= -1.25 \pm 0.01$ (~ -1.15) in SMC (LMC) star clusters (Cioni 2009), while the MW metallicity distribution peaks around solar values

We note that the free broken power law with MW-type extinction curve cannot be formally excluded by the fit ($\chi^2_\nu = 2.99$ for 146 d.o.f.). However, the very low dust content implied by this solution [$E(B - V) = 0.008 \pm 0.007$] also suggests a low metallicity for the absorbing gas (e.g. Vladilo 1998).

N(H) cannot be constrained, i.e. it is consistent with the Galactic value and with the large error of the X-ray-only N(H) $= 15.5^{+13.9}_{-14.9} \times 10^{20}$ cm^{-2}. This N(H) falls at the low end of the N(H) distribution of GRB afterglows (e.g. Evans et al. 2009; Fynbo et al. 2009; Campana et al. 2010), and A_V also falls at the low end of the dust extinction distribution (e.g. Kann et al. 2010; Schady et al. 2011; Zafar et al. 2011). The dust-to-gas ratio N(H)$/A_V = 3.1^{+2.7}_{-3.0} \times 10^{22}$ cm^{-2} mag^{-1} covers most of the GRB N(H)$/A_V$ distribution at its low end (see Zafar et al. 2011) and is similar to GRB 980329 (Starling et al. 2007). In fact, one in every six *Swift* XRT X-ray afterglows has unconstrained excess N(H) (Evans et al. 2009), given the difficulty of measuring low host galaxy N(H) against higher Galactic N(H) and its uncertainties.

At earlier epochs I and II, the afterglow SED is affected by flaring activity. This is most evident in the V and R bands where epochs I and II coincide with the rise and decay of a flare or bump in the light curves (Fig. 1). For completeness we report individual fits to these early epochs in Appendix A. Our NIR-to-X-ray SED results are in overall agreement with the single-epoch SED at 4.3 d previously analysed by Updike et al. (2008). In particular, we confirm the presence of a spectral break. This break was only tentatively found by Updike et al. (2008), because of its sensitivity to the NIR continuum level, based on a large extrapolation of solely two data points in the K band. In our data set, six additional NIR data points were added, i.e. K_s, J, H from the SMARTS telescope (Kann et al. 2010) and K_s, J, H from the PAIRITEL telescope (from GCN, Chandra et al.

both in the bulge (e.g. Zoccali et al. 2003) and in the thin disc (Tiede & Terndrup 1999), covering the majority of the stellar population.

2008). Moreover, no extrapolations were needed for the NIR light curve from epochs III to V of our SED fit. Finally, the significant improvement from a single power-law SED fit to a broken power law strongly favours the presence of the spectral break.

5.2 The broad-band picture

To determine the full set of physical parameters of a GRB afterglow, it is vital to have good temporal and spectral coverage from X-ray to radio frequencies. GRB 070125 is a good candidate for this kind of study, in particular because of its coverage at centimetre wavelengths. With well-sampled light curves at multiple radio observing frequencies, one can determine the evolution of the peak flux, the associated peak frequency ν_m and the synchrotron self-absorption frequency ν_a. Together with the cooling frequency ν_c, the electron energy distribution index p and the jet-break time, all the microphysical and macrophysical parameters of the GRB jet and its surroundings can be pinned down. For GRB 070125 this has been done by Chandra et al. (2008) for part of the total available data set. Updike et al. (2008) have focused their modelling efforts mainly on the optical and X-ray regimes, as we have done in Section 5.1. There are some inconsistencies between the different modelling results, and complications in interpreting the full data set, which we will discuss here.

The main issue is the position of the cooling break in the broad-band spectrum. Our SED fits show that there is a spectral break between the optical and X-ray bands. The spectral slope differences between the two bands indicate that this break can be interpreted as the cooling break. As pointed out by Updike et al. (2008), it is difficult to form a coherent picture of these spectral slopes and the temporal slopes observed at optical and X-ray frequencies within the standard afterglow framework, because not all the so-called closure relations (e.g. Zhang & Mészáros 2004) can be satisfied. Updike et al. (2008) suggested a solution for this issue by adopting that the NIR-to-X-ray SED is in fact a single power law, and they concluded that all those observing bands are in between ν_m and ν_c and that the circumburst medium is homogeneous. This solution is not satisfactory given that we confirm the presence of a cooling break in the NIR-to-X-ray SED, similar to what was found and tentatively discarded by Updike et al. (2008).

A complicating factor is the flaring behaviour of GRB 070125, which makes reliable determinations of temporal slopes difficult. Our SEDs have been constructed at times when the flaring has ceased, but leaving out the flaring parts of the optical and X-ray light curves gives a relatively short lever arm for determining the temporal slopes, in turn giving rise to large statistical and systematic uncertainties. This could account for the fact that the standard closure relations for ν_c in between the optical and X-ray bands do not seem to work. For example, it is mentioned in Updike et al. (2008) that the optical temporal slopes are consistent with the spectral slopes if the circumburst medium is structured like a stellar wind, but the X-ray temporal slope is inconsistent. The latter could be due to uncertainties caused by the flaring of the source. The bottom line is that in the case of GRB 070125 the NIR-to-X-ray SED fits seem to give the most reliable measurement of the value of ν_c.

The broad-band SED fitting performed by Chandra et al. (2008), including the centimetre wavelength radio data, leads to different conclusions. They find that the optical and X-ray regimes lie on the same power-law segment of the synchrotron spectrum, but above both ν_m and ν_c. In fact, one of the outcomes of their modelling is that this afterglow is in the fast cooling regime, i.e. $\nu_c < \nu_m$, for about a week, which has not been observed in any GRB afterglow before.

The values for p they find result in optical and X-ray spectral indices of ~ 1.1–1.2. These indices are consistent with the X-ray spectral index we find in our SED fitting, but inconsistent with the shallower optical indices we find, and also the indices obtained by Updike et al. (2008) for NIR–optical SED fits. The uncharacteristically low value for ν_c is necessary to describe the optical and X-ray light curves together with the bright and long-lasting radio afterglow. If ν_c would be at higher frequencies, there is no possible combination of ν_a, ν_m and the peak flux to give a satisfactory fit of the radio data. Although the modelling performed by Chandra et al. (2008) is thorough, the basic assumptions are fairly simplified. To get to a coherent solution for all the broad-band data, a more complicated picture may have to be invoked, like a double jet as has been suggested for the broad-band afterglow of, e.g., GRB 030329 (Berger et al. 2003). Another possibility is that we need a more detailed description of the afterglow physics, in particular the effects of synchrotron self-absorption on the jet-break time at radio wavelengths and the associated changes this makes to radio light curves (van Eerten et al. 2011). These different, more complicated scenarios for satisfactorily describing the full data set of GRB 070125 are beyond the scope of this work, but will be explored and presented in a future paper.

While the broad-band modelling needs further study, we can still rely on the NIR-to-X-ray SED, as it is based on fewer assumptions. In particular, we found a low $N(H)$ and a low SMC/LMC-type dust content, suggesting a low-metallicity environment.

5.3 The absorber environment

While the broad-band SED depends on the afterglow physics and the circumburst environment, the absorption in the optical spectrum probes the gas along the line of sight. By studying the nature of the absorber, we can derive information on the GRB site, as we will discuss here.

A crucial issue that needs to be addressed is whether or not the Mg II absorbing system observed in the afterglow spectrum is associated with the host galaxy of GRB 070125. While a host galaxy could, in principle, be in the background at a larger redshift, we note that Lyα absorption at $z \gtrsim 1.9$ [7] would be observable in our high S/N FORS spectra, but no signature of such system was detected. Fig. 5 shows how the observed GRB 070125 FORS spectrum compares to the GRB composite spectrum from Christensen et al. (2011) at the same redshift $z = 1.5477$. A $1.5 \lesssim z \lesssim 1.9$ host galaxy could be possible but no lines are detected at such redshift. Thus, we consider $z = 1.5477$ to be the host galaxy redshift. A tentative Lyα absorption at this redshift was reported by Updike et al. (2008), for which $\log N(H I) < 20.3$ was argued. We note that high-ionization N V $\lambda\lambda 1238$, 1242 Å lines are not in our wavelength reach. No spectroscopic observation has been attempted to investigate the two candidate blue hosts that Cenko et al. (2008) indicated at a large offset from the GRB position so far. Below we will discuss the possible scenarios.

The metallicity along the GRB 070125 line of sight cannot simply be constrained from the measured column densities or upper limits, since no Lyα is available in our FORS spectra, given the redshift of this afterglow. One way to bypass the lack of $N(H I)$ measurement is plotting $[X/H I] + \log N(H I) = \log N(X) - \log N(X)_\odot + \log N(H I)_\odot$, as in Fig. 6. Despite the degeneracy between H I

---

[7] Corresponding to the bluest observable wavelength $\lambda = 3515$ Å in the spectrum cut where S/N ~ 10.
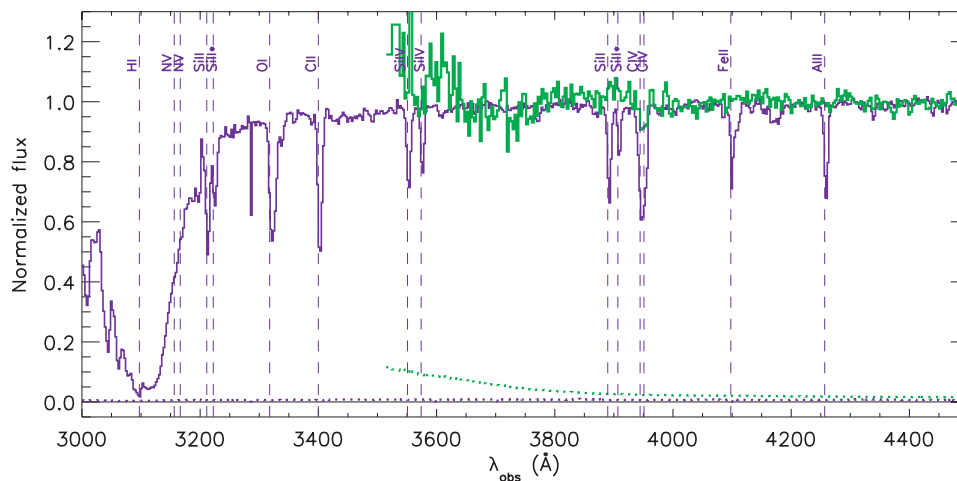
Figure 5. The high S/N GRB composite spectrum (dark) from Christensen et al. (2011) shifted to $z = 1.5477$ and the observed GRB 070125 FORS spectrum (light) cut at S/N > 10. The error spectra are shown by the dotted lines. A firm upper limit of $z \lesssim 1.9$ can be placed on the GRB 070125 redshift from the lack of Lyα forest lines in the afterglow spectrum.
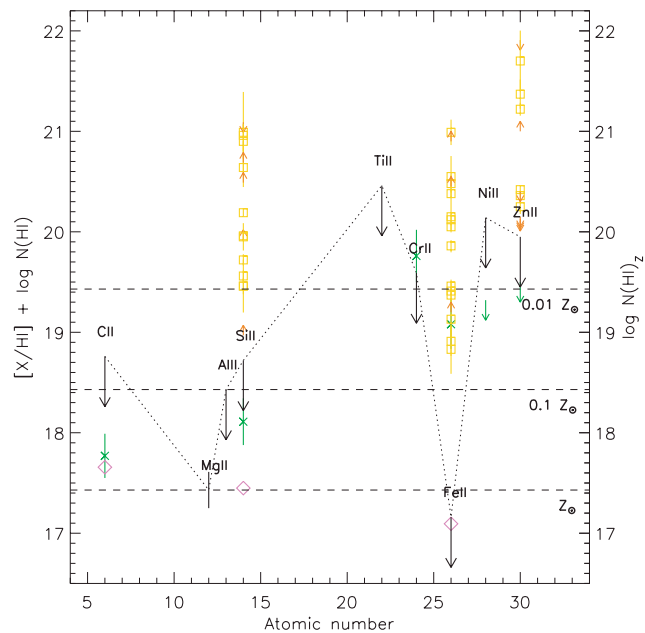
Figure 6. Abundances and 3σ detection limits of a selection of low-ionization species in the GRB 070125 afterglow spectrum (black bar and arrows) from Tables 2 and 3. The ordinate combines the metallicity and the H I column density, basically a measure of the metal abundances with respect to solar, in order to show the possible ranges of metallicity and $N(\text{H I})$ in the absorber. The horizontal dashed lines correspond to the neutral hydrogen column density for a given metallicity, $\log N(\text{H I})_Z$, with respect to the Mg II detection, assuming no depletion of Mg into dust. Light-coloured squares and arrows show the metal abundances observed in GRB absorbers (Schady et al. 2011) and the crosses refer to the GRB 080310 measurements (De Cia et al., in preparation). The column density expectations (diamonds) for the measured Mg II are derived from the correlations observed in weak Mg absorbers (Narayanan et al. 2008).

column density and metallicity, we can use the Mg II detection and the upper limits to explore the parameter space and at least limit the possible $N(\text{H I})$ and [X/H I]. In particular, assuming solar metallicity and no Mg depletion into dust, we derive $\log N(\text{H I}) = 17.43$. If the metallicity is 1/100 solar then $\log N(\text{H I}) = 19.43$. A much lower

metallicity is very hard to justify, while a supersolar metallicity with lower $N(\text{H I})$ is possible. Hence, we can reduce the possibilities for the GRB 070125 absorber to be either (i) a sub-Lyman limit system [sub-LLS, $\log N(\text{H I}) < 17.3$; Rauch 1998] with $Z > 1.3\,Z_\odot$, or (ii) an LLS [$17.3 < \log N(\text{H I}) < 19.0$; Péroux et al. 2003] with $0.03 < Z < 1.3\,Z_\odot$, or (iii) a sub-damped Lyα absorber [sub-DLA; $19.0 < \log N(\text{H I}) < 20.3$] with $0.001 < Z < 0.03\,Z_\odot$. Below we discuss these three different scenarios.

(i) *A supersolar Z sub-LLS.* This scenario is supported by the low Mg II EW of GRB 070125, since the majority of weak Mg II (EW < 0.3 Å) absorbers in quasar lines of sight are associated with sub-LLS with supersolar metallicity (Churchill et al. 1999). This association is based on the number density consistency between the two populations and a CLOUDY photoionization model that predicts $\log N(\text{H I}) < 17.3$ for weak Mg II. Given the observed Mg II column density in GRB 070125, the C II, Si II and Fe II expectations for weak Mg II systems derived by Narayanan et al. (2008) (diamonds in Fig. 6) are consistent with our upper limits. These systems could trace either interstellar gas expelled from star-forming regions into the halo, or small clouds in dwarf galaxies or intergalactic star-forming structures (Churchill et al. 1999). The least likely possibility is the GRB explosion site in the halo. Cenko et al. (2008) already pointed out the difficulty of explaining how to 'kick' the massive GRB progenitor star all the way out to the galaxy halo ($\sim$27 kpc). A halo *in situ* formation of the GRB would require halo gas at $\sim$27 and 46 kpc from two interacting galaxies to trigger massive star formation, the GRB progenitor producing high-density stellar winds to 'fuel' the extremely bright afterglow ($n \approx 50\,\text{cm}^{-3}$; Chandra et al. 2008). One other possibility is that the GRB exploded in a dwarf galaxy. Ellison et al. (2004) studied the Mg II systems coherence length, indicating that the weak Mg II absorbers have sizes of 1.5–4.4 kpc and they could represent a distinct population of smaller galaxies. However, the low content of SMC/LMC-type dust from the GRB 070125 afterglow SED suggests a low metallicity of the host galaxy, disfavouring the supersolar Z sub-LLS scenario.

(ii) *A $0.03 < Z < 1.3\,Z_\odot$ LLS.* Although GRB absorbers show, on average, high H I column densities (e.g. Jakobsson et al. 2006), an LLS is not an exotic environment for a GRB, since a low $N(\text{H I})$ may be a line-of-sight effect. In principle, the burst radiation can

travel along the line of sight, within the host galaxy or from the galaxy outskirts, without being absorbed by dense gas clouds. This scenario is supported by the observation of a few other GRB LLSs, namely GRB 050908 [$\log N(\mathrm{H\,I}) = 17.60 \pm 0.10$; Fugazza et al. 2005; Fynbo et al. 2009], GRB 060124 [$\log N(\mathrm{H\,I}) = 18.5 \pm 0.5$; Prochaska et al. 2006; Fynbo et al. 2009], GRB 060607A [$\log N(\mathrm{H\,I}) \sim 16.8$; Ledoux et al. 2006; Prochaska et al. 2008], GRB 080310 [$\log N(\mathrm{H\,I}) = 18.70 \pm 0.10$; De Cia et al., in preparation) and GRB 090426 [$\log N(\mathrm{H\,I}) = 18.70^{+0.1}_{-0.2}$; Thöne et al. 2011], where Lyα variability was induced by H I ionization. The low H I content of all these systems cannot be explained by ionization alone, as the burst radiation can totally ionize H I only out to 200–300 pc[8] from the burst in LLSs (using the bright GRB 050730 afterglow light curve; Ledoux et al. 2009). A low H I could arise if the GRB is not too deeply embedded in its host galaxy. Such a possibility, which is certainly expected in some cases, will be further investigated later on in this section.

The equivalent hydrogen column density measured from the soft X-ray absorption can also provide important information on the gas along the line of sight, with the advantage of not depending on the H I ionization. Indeed, $N(\mathrm{H\,I})$ and $N(\mathrm{H})$ do not correlate (Watson et al. 2007; Campana et al. 2010). The difference between a low neutral and a high total hydrogen column densities can be explained if most of the X-ray absorbing gas lies closer to the burst, where the gas is highly ionized (Schady et al. 2011). In this scenario, the GRB 070125 could still have been surrounded by the high-density gas required to power such a bright afterglow.

(iii) *A* $0.001 < Z < 0.03 \, Z_\odot$ *sub-DLA.* This metallicity range is low, but not unusual for GRB absorbers. For instance, most of the GRB absorbers in the VLT/UVES sample have $0.006 < Z < 0.05 \, Z_\odot$, despite the small number statistics (Ledoux et al. 2009), although their H I column densities are generally higher.

From the above analysis, scenarios (ii) and partly (iii) are favoured, i.e. the GRB 070125 environment is consistent with other GRBs. Below we test this further, by comparing the GRB 070125 properties with the GRB population.

In Fig. 6 we compare the measured metal column densities and upper limits for GRB 070125 with those observed in other GRB afterglows (squares and arrows), as collected by Schady et al. (2011). The metal column densities in GRB 070125 are generally lower than those measured in other GRBs. This suggests that the GRB 070125 absorber has either a lower metallicity or a lower H I column density with respect to most GRBs. However, this comparison sample is limited, since the column densities often cannot be constrained, due to the low resolution of the spectra, and more complete EW distributions should be used. The EW of C IV $\lambda1549$ in GRB 070125 is EW$_{rest}$ = 0.77 ± 0.09 Å, much lower than in the GRB composite spectrum (EW$_{rest}$ = 2.18 ± 0.03 Å; Christensen et al. 2011) and in the low H I afterglow subsample (EW$_{rest}$ $\sim$ 2.8 Å; Thöne et al. 2011). Nevertheless, the observed C IV $\lambda1549$ EW and the Si II $\lambda1526$ upper limit are consistent with the EW correlation found in Fynbo et al. (2009). This suggests that the GRB 070125 absorber fits in the GRB population, rather than being an outlier. In Fig. 7 we compare the C IV $\lambda\lambda1548$, 1550, Mg II $\lambda2796$ EWs and the deep Fe II $\lambda2382$ 3σ detection limit for GRB 070125 with the EW distributions discussed by de Ugarte Postigo et al. (in preparation) for the whole low-resolution spectroscopy afterglow sample of Fynbo et al. (2009). The GRB 070125 absorber falls in the low end of the EW

[8] For much brighter afterglows, these distances can significantly grow; see our discussion below.
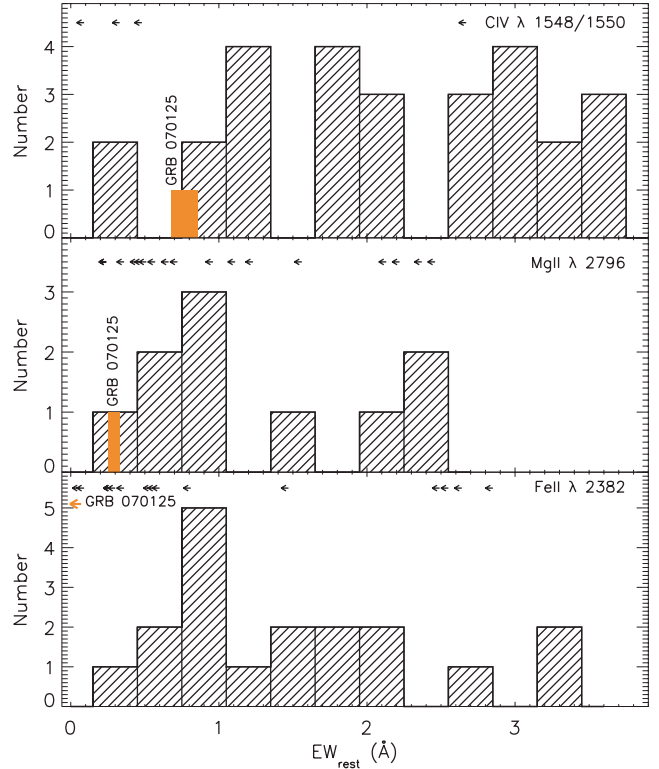
Figure 7. The C IV $\lambda1548/1550$, Mg II $\lambda2796$ and Fe II $\lambda2382$ rest-frame EW distributions for GRB absorbers. The EW and 3σ detection limits are taken from de Ugarte Postigo et al. (in preparation) and based on Fynbo et al. (2009). The highlighted GRB 070125 EWs fall at the low end of the EW distribution.

distribution. Again, this indicates that GRB 070125 is not a GRB population outlier and that other bursts share similar properties.

Furthermore, we selected two afterglow subsamples that may potentially be similar to GRB 070125: (a) the spectral-line poor, i.e. afterglows with no more than two species in absorption at the GRB redshift, selected from Fynbo et al. (2009) and (b) afterglows with low equivalent hydrogen column density $N(\mathrm{H})$ measured from the X-rays, $N(\mathrm{H}) < 5 \times 10^{21}$ cm^{-2}, within 3σ. $N(\mathrm{H})$ and A_V were collected from Zafar et al. (2011) when possible, otherwise the $N(\mathrm{H})$ from Evans et al. (2009) and the A_V from Kann et al. (2010) were used. The $N(\mathrm{H\,I})$ were taken from Fynbo et al. (2009) and the EWs from de Ugarte Postigo et al. (in preparation), with the exception of GRB 060708 and GRB 080310, whose metal EWs are measured here. We exclude the low S/N spectra from the spectral-line poor sample by applying a cut in the Mg II $\lambda2796$ detection limit of $\sigma_{EW} <$ 0.5. The low S/N spectra are also excluded from the EW constraints of the low $N(\mathrm{H})$ subsample. Six afterglows fall in our spectral-line poor subsample, not including GRB 070125, listed in Table 5, while 15 are in the low $N(\mathrm{H})$ subsample.

We note that the spectral-line poor subsample may suffer from selection effects. First, afterglows with low redshift ($z \leq 0.5$) may more easily be included in this subsample because of the shortage of observable transitions (other than the Mg II $\lambda\lambda2796$, 2803 doublet) in the spectral region covered by typical optical spectrographs. However, only two GRBs have such low z in Table 5. Secondly, the S/N requirement may bias the subsample towards brighter bursts. This is irrelevant when comparing the subsample properties with GRB 070125, the latter being very bright itself, but should be kept in mind when considering the spectral-line poor subsample as a

Table 5. Spectral-line poor sample (first group, based on the Fynbo et al. 2009, sample) and related cases (second group, not included in the Fynbo et al. 2009, sample).

GRB	z	R_c^a (Mag$_{acq}$)^b (mag)	Underlying host absolute (apparent) magnitude	Notes	References
060607A	3.07	(14.0)	$M_{AB}(780\,nm) > -20.14$	$\log N(\mathrm{H\,I}) = 16.85 \pm 0.10$	1, 2, 3
060614	0.13	24.04 ± 0.05	$M_B = -15.5$	Host $\log M/M_\odot = 7.95$	1, 4, 5
060708	1.92	(22.9)	?^{c}	Photometric redshift (low S/N)	
060908	1.88	22.5 ± 0.5	$(R \sim 25.6)$		1, 6
061021	0.35	(20.5)	Detected	Redshift from host and afterglow	7
070419A	0.97	23.1 ± 0.5	?		
070125	1.55	17.5 ± 0.1	$M(780\,nm) > -18.5$		8
071003	1.60	17.7 ± 0.1	$M(K') > -22.2$	Halo environment claimed	9
101219B	0.55	(19.8)	$(r = 23.7 \pm 0.2^d)$	Associated SN	10

^{a}Afterglow brightness at 1 d after the burst, shifted to $z = 1$ (Kann et al. 2010, 2011); ^{b}R, i or z afterglow brightness from the acquisition images of the spectra (Fynbo et al. 2009); ^{c}no observations available; ^{d}possible contribution from the SN or the afterglow itself.
References. (1) Savaglio, Glazebrook & Le Borgne (2009); (2) Chen et al. (2009); (3) Laskar, Berger & Chary (2011); (4) Della Valle et al. (2006); (5) Gal-Yam et al. (2006); (6) Covino et al. (2010); (7) Fynbo et al. (2009); (8) Cenko et al. (in preparation); (9) Perley et al. (2008); (10) Sparre et al. (2011).

population. A more extended and complete sample with deeper S/N limits is needed to further analyse and possibly exclude these selection effects.

Fig. 8 shows a comparison of the GRB 070125 afterglow absorber properties with the two subsamples. GRB 070125 traces the low end of the $N(\mathrm{H})$, A_V and EW distributions, confirming the previous finding for the whole sample.

In general, we note that most of the spectral-line poor afterglows also show a low $N(\mathrm{H})$. The few low $N(\mathrm{H})$ afterglows with Lyα measurements seem to prefer low H I environment, although no conclusion can be drawn yet due to the extremely poor statistics. The same applies to the lack of high EW at constrained low $N(\mathrm{H})$. The above suggestions, if confirmed, may indicate an overall low column density environment for both the low-ionization gas (that absorbs the metal lines in the optical spectrum at distances larger than a few hundred pc from the burst) and the highly ionized gas (that absorbs the soft X-rays, in the vicinity of the burst). More observations are needed to investigate whether $N(\mathrm{H})$ and $N(\mathrm{H\,I})$ could correlate under special conditions, e.g. due to the effect of a short line of sight within the host galaxy, despite there generally being no such correlation. However, we note that the $N(\mathrm{H})$ typically cannot be constrained below $\log N(\mathrm{H}) < 20$–21, due to the uncertainty in the Galactic $N(\mathrm{H})$.

One GRB absorber potentially similar to GRB 070125 is the recent nearby GRB 101219B, with redshift $z = 0.55$ identified from the Mg II $\lambda\lambda2796$, 2803 and Mg I $\lambda2853$, the only features in the afterglow spectrum. A spectroscopically confirmed supernova was associated with this GRB, supporting both the low redshift and a massive star progenitor for the GRB. The afterglow spectral shape suggested a very low amount of dust ($A_V < 0.1$), while the non-detection of the host galaxy continuum or emission lines indicated that a small galaxy was hosting the GRB, at the faint end of the Savaglio et al. (2009) distribution (Sparre et al. 2011).

Another case analogous to GRB 070125 was GRB 071003, a very bright burst ($R \approx 12$ mag about a minute after trigger), with a few and very weak absorption lines in the late-time spectrum and no underlying bright host. Given the similarity between the two, GRB 071003 was also claimed to have occurred in a halo environment (Perley et al. 2008). In both cases, while the high brightness of the afterglow cannot easily be associated with a halo star-forming region, it can naturally contribute to ionize the circumburst medium to larger distances. And perhaps the time delay between the burst and the epoch of the spectra ($\sim$1 d in both cases) could allow the ionization front of the bright afterglow to travel further through the host galaxy.

In order to investigate this possibility, we performed a simplified simulation of the GRB 070125 afterglow radiative effect on the surrounding medium with a radiative transfer model, including photoionization. A detailed description of the complete model will be discussed in Vreeswijk et al. (in preparation). We use the GRB 050730 light curve as a template, scaled to the 3.3 times brighter flux of GRB 070125 [derived from the afterglow brightness at 1 d, if both GRBs would lie at $z = 1$, R_c (GRB 050730) $-R_c$ (GRB 070125) = 1.3 mag; Kann et al. 2010]. We assume a spectral slope $\beta = 0.7$, as before the synchrotron cooling, since the most relevant photons are the UV in the first hours after the burst. We let the GRB afterglow radiate through a cloud lying at a distance between 0 and 2 kpc and investigate the variation of the ionic column densities. In general, most of the GRB absorbers have been found to lie within this distance range from the burst, in those cases for which the GRB-to-cloud distance could be estimated from the variability of fine-structure lines in the spectra. Two different sets of initial column densities were chosen: (a) $N(\mathrm{H\,I}) = 10^{19}$ cm^{-2} and $N = 10^{14}$ cm^{-2} for the metal ions and (b) $N(\mathrm{H\,I}) = 10^{20}$ cm^{-2} and $N = 10^{15}$ cm^{-2} for the metals. We set the observation times to be at 1 d and 6 h for comparison (observer frame). The results for case (a) are displayed in Fig. 9. While the higher $N(\mathrm{H\,I})$ shields the metals from being ionized at large distances, in the case of $N(\mathrm{H\,I}) = 10^{19}$ cm^{-2} most of the metals are strongly ionized out to $\sim$0.5 kpc. In particular, at 0.5 kpc the Mg II column density is 10 times lower than the initial value, Fe II is $\sim$30 times lower than the initial column, Ni II even lower. The late time of the spectrum (1 d) does not seem to be an important factor, as the comparison with the ionization expected at 6 h after the burst does not change the result dramatically. In particular, Mg II and Fe II are ionized by only a factor of $\sim$2 between 6 and 24 h, indicating that most of the ionization is happening within the first hours after the burst. At 0.2 kpc all these metals and H I are totally ionized. Thus, we
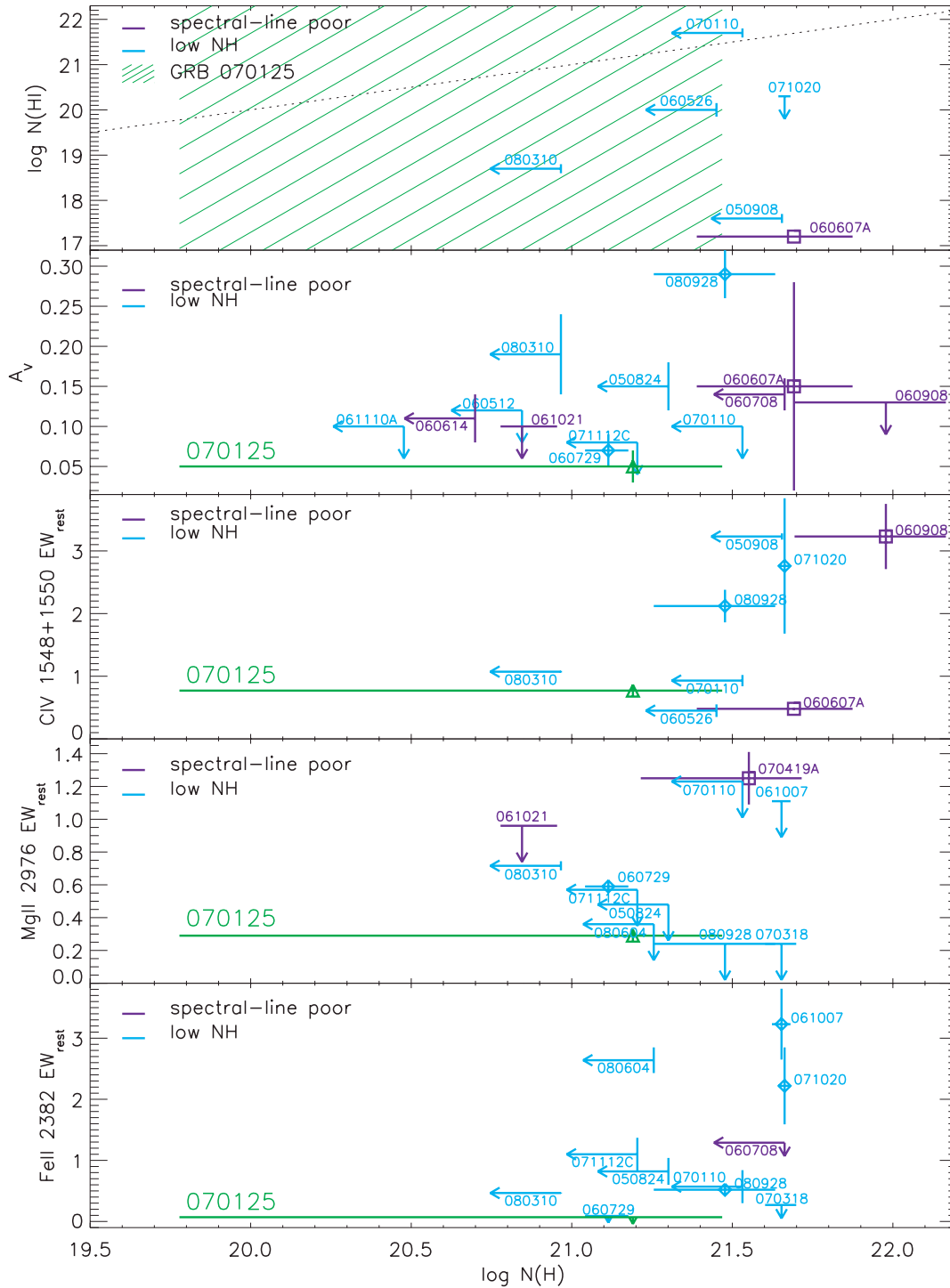
Figure 8. The neutral hydrogen column density, dust extinction and rest-frame EWs versus the equivalent hydrogen column density of the spectral-line poor (dark) and the low N(H) (light) GRB subsamples. The GRB 070125 properties are highlighted. The dotted line in the top panel marks where N(H) and N(H I) are equal. We do not display the four highest A_V values ($0.34 < A_V < 0.49$) at the high N(H) distribution end, in order to focus on the low A_V and N(H) cases most similar to GRB 070125. A complete N(H) versus A_V distribution is presented in Zafar et al. (2011).

conclude that any cloud within 0.5 kpc would not be visible, in terms of spectral lines of low-ionization species. This evidence, together with a GRB location not too deep inside the host galaxy (i.e. within 0.5 kpc), can explain the lack of spectral features in the spectrum of GRB 070125.

The feasibility of this scenario for other bursts can be tested by comparing how many cases similar to GRB 070125 we expect and how many we actually observe. For a zero-order approximation, we calculate the rough probability of a GRB to have (i) a short line of sight within the host galaxy, (ii) a low absorbing N(H I) and (iii)
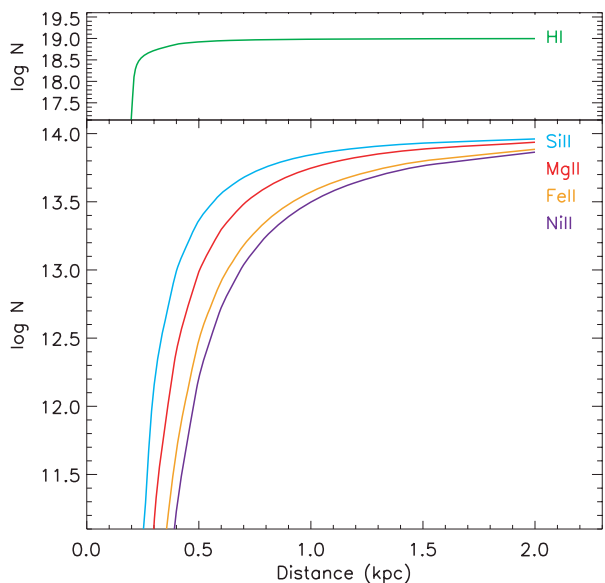
Figure 9. The ionization effect of the afterglow radiation on absorbing clouds at a given distance with initial column densities $\log N(\text{H\,\textsc{i}}) = 19$ and $\log N = 14$ for the metals, as observed at 1 d after the burst. See text for details.

a bright afterglow. (i) The probability of a GRB to be located not deeper than 0.5 kpc within its host galaxy depends on the galaxy size [in one simple dimension it can be simplified as $p(<0.5\,\text{kpc}) \approx 0.5\,\text{kpc size}^{-1}$]. Integrating this probability over a normal distribution of GRB host galaxy sizes centred around the mean size 2.4 kpc (Wainwright, Berger & Penprase 2007, assuming $\sigma = 0.8$ and excluding sizes below 0.5 kpc, to reproduce the observed 0.5–5 kpc size distribution) provides a 22 per cent chance of a GRB line of sight traversing less than 0.5 kpc of its host galaxy.[9] (ii) Among the GRB absorbers with detected Lyα absorption in the Fynbo et al. (2009) sample, 15 per cent are LLS or lower $N(\text{H\,\textsc{i}})$. (iii) The afterglow brightness distribution, scaled to redshift $z = 1$ and at 1 d after the burst, is presented in Kann et al. (2010), providing 16 per cent of GRBs with $R_c < 18$ mag afterglows. A different approach, considering the magnitudes of the acquisition images (R-, i- or z-band magnitude) of the afterglow spectra from Fynbo et al. (2009), yields 12 per cent afterglows with $\text{Mag}_{\text{acq}} < 18$ mag. Combining the three probabilities above, we estimate that about 0.5 per cent of all GRB afterglows are similar to GRB 070125, i.e. spectral-line poor and bright. This is somewhat consistent with the observations of GRB 070125, GRB 060607A and including GRB 071003, the three of them representing 4 per cent of the afterglows analysed in Kann et al. (2010). We made an approximate estimate of the number of GRBs with a ground-based detection among the *Swift* sample (and hence the possibility of being identified as spectral-line poor, low $N(\text{H\,\textsc{i}})$ and optically bright), using the *Swift* GRB table.[10] This results in 324 GRBs up to 2011 May 1, of which 1 per cent would mean approximately three sources, again consis-

[9] This estimate assumes a random distribution of the GRB locations inside the host galaxy. However, the low-metallicity requirement for the GRB progenitor formation (e.g. Hirschi, Meynet & Maeder 2005) would increase the probability of GRBs being located in the outskirts of their hosts, given the typical metallicity gradients.
[10] http://swift.gsfc.nasa.gov/docs/swift/archive/grb_table/

© 2011 The Authors, MNRAS **418**, 129–144
Monthly Notices of the Royal Astronomical Society © 2011 RAS

tent with current observations. If we relax the brightness requirement, about 3 per cent of all GRB afterglows are expected to have a low $N(\text{H\,\textsc{i}})$ and lie in the outer kiloparsec of their host galaxy along our line of sight. The nine spectral-line poor afterglows listed in Table 5 (including GRB 071003 and GRB 101219B) represent 12 per cent of the afterglows of Kann et al. (2010), or 3 per cent of the *Swift* optical/IR afterglows. It is possible that these spectral-line poor afterglows are the result of a GRB location in the outer regions of their host galaxy and a low $N(\text{H\,\textsc{i}})$. Further investigations are needed to confirm these results.

Finally, we point out that the non-detection of the GRB 070125 host galaxy in the KeckI/Low Resolution Imaging Spectrometer (LRIS) images down to $R > 25.4$ mag (Cenko et al. 2008) is consistent with a $M_{300,\,\text{AB}} > -18.8$ galaxy at $z = 1.5477$ (k-corrected AB magnitude at 300 nm), i.e. a faint (among the 25 per cent faintest) but still not uncommon GRB host galaxy at that redshift (Schulze et al., in preparation). Indeed, GRB hosts are generally faint irregular galaxies (Savaglio et al. 2009). Recent *Hubble Space Telescope* imaging of the field provides deeper upper limits on the host brightness of $F336W > 26.7$ mag (AB) (central wavelength $\lambda_c \sim 334.4$ nm) and $F110W > 26.4$ mag ($\lambda_c \sim 1123.8$ nm), not corrected for foreground extinction (Cenko et al., in preparation). We then correct for Galactic foreground extinction of 0.26 and 0.05 mag in the $F336W$ and $F110W$ bands, respectively. The former upper limit corresponds to an absolute brightness of $M_{300,\,\text{AB}} > -18.3$ mag in the 300-nm rest frame, assuming $F_\nu \propto \nu^{-1/2}$ at that wavelength. The NIR observation in $F110W$ can constrain the rest-frame optical/NIR brightness of the host galaxy, mostly attributed to late-type stars and the old stellar population. The upper limit corresponds to $M > -18.2$ mag in the 780 nm, assuming $F_\nu \propto \nu^{-1/2}$. As is the case in the UV, this host is among the faintest hosts in the luminosity distributions of Savaglio et al. (2009) and Laskar et al. (2011).

6 SUMMARY AND CONCLUSIONS

We collected all observational data of GRB 070125 available in the literature, in order to investigate the environmental properties of the burst, and in particular to test the putative halo origin of this burst based on the few weak absorption lines in the spectrum and the absence of an underlying bright host (Cenko et al. 2008).

The NIR-to-X-ray SED at 1.9, 2.5 and 2.9 d after the burst revealed a synchrotron cooling break in the UV. Along the line of sight in the host galaxy, little reddening [$E(B - V) = 0.016 \pm 0.007$] is caused by an LMC- or SMC-type dust, while a low equivalent hydrogen column density cannot be constrained better than $N(\text{H}) = 15.5^{+13.9}_{-14.9} \times 10^{20}\,\text{cm}^{-2}$. The NIR-to-X-ray SED results are inconsistent with broad-band SED analyses including radio observations, indicating that the assumptions in modelling efforts for GRB 070125 so far have probably been too simplified. More complex afterglow models should be explored, in particular to unify the light curves across the broad-band spectrum with the NIR-to-X-ray SED.

The analysis of the high S/N, but rather featureless FORS spectrum showed weak Mg\,\textsc{ii} and C\,\textsc{iv} in absorption, providing $\log N(\text{Mg\,\textsc{ii}}) = 12.96^{+0.13}_{-0.18}$. The constraint on the Mg\,\textsc{ii} column density, together with the upper limits for the other ions and the evidence for low metallicity from the SED, suggested that the GRB absorber is most likely a $0.03 < Z < 1.3\,\text{Z}_\odot$ LLS, also observed along the line of sight to five other GRBs. The comparison of the GRB 070125 measurements with the rest-frame EWs of the GRB afterglow sample of Fynbo et al. (2009) revealed that GRB 070125

is not unique, but simply falls at the low end of the EW distribution. Furthermore, we selected two subsamples of afterglows possibly similar to GRB 070125, the spectral-line poor and the low N(H). Most spectral-line poor afterglows show a low A_V and low N(H), suggesting that a short distance in the host galaxy is traversed by the line of sight. In any case, a quite featureless spectrum is not as uncommon for GRB afterglows as previously claimed.

We demonstrated that the few and weak features in the spectrum of GRB 070125 can be the result of the particularly intense afterglow radiation ionizing a low $\log N$(H I) $\sim$ 19 through a line of sight traversing not more than about 0.5 kpc of its faint host galaxy. We showed that the few and weak spectral features are not so uncommon in GRB afterglows, including the nearby GRB 101219B at $z =$ 0.55, with associated SN, for which a subluminous host galaxy has been claimed. Finally, the non-detection of a host galaxy at the GRB 070125 position indicates that an underlying galaxy, if present, must be among the faintest GRB host galaxies.

Given that about half of the GRBs in the spectral-line poor subsample have a detected host galaxy, it seems likely that these bursts are also located in the outskirts of a gas-rich, massive star-forming region inside its small and faint host galaxies, rather than in a halo environment.

ACKNOWLEDGMENTS

REFERENCES

Appenzeller I. et al., 1998, The Messenger, 94, 1
Arnaud K. A., 1996, in Jacoby G. H., Barnes J., eds, ASP Conf. Ser. Vol. 101, Astronomical Data Analysis Software and Systems V. Astron. Soc. Pac., San Francisco, p. 17
Asplund M., Grevesse N., Sauval A. J., Scott P., 2009, ARA&A, 47, 481
Bellm E. C. et al., 2008, ApJ, 688, 491
Berger E. et al., 2003, Nat, 426, 154
Björnsson G., Gudmundsson E. H., Jóhannesson G., 2004, ApJ, 615, L77
Burrows D. N. et al., 2005, Space Sci. Rev., 120, 165
Campana S., Thöne C. C., de Ugarte Postigo A., Tagliaferri G., Moretti A., Covino S., 2010, MNRAS, 402, 2429
Cenko S. B., Fox D. B., 2007, GRB Coordinates Network, 6028
Cenko S. B. et al., 2008, ApJ, 677, 441
Chandra P. et al., 2008, ApJ, 683, 924
Chen H.-W. et al., 2009, ApJ, 691, 152
Christensen L., Fynbo J. P. U., Prochaska J. X., Thöne C. C., de Ugarte Postigo A., Jakobsson P., 2011, ApJ, 727, 73
Churchill C. W., Rigby J. R., Charlton J. C., Vogt S. S., 1999, ApJS, 120, 51
Cioni M., 2009, A&A, 506, 1137
Covino S. et al., 2010, A&A, 521, A53
Dai X. et al., 2008, ApJ, 682, L77
de Ugarte Postigo A. et al., 2005, A&A, 443, 841
Della Valle M. et al., 2006, Nat, 444, 1050
Dickey J. M., Lockman F. J., 1990, ARA&A, 28, 215
Ellison S. L., Ibata R., Pettini M., Lewis G. F., Aracil B., Petitjean P., Srianand R., 2004, A&A, 414, 79
Evans P. A. et al., 2007, A&A, 469, 379
Evans P. A. et al., 2009, MNRAS, 397, 1177
Fox D. B., Berger E., Price P. A., Cenko S. B., 2007, GRB Coordinates Network, 6071
Fugazza D. et al., 2005, GRB Coordinates Network, 3948
Fynbo J. P. U. et al., 2006, A&A, 451, L47
Fynbo J. P. U. et al., 2009, ApJS, 185, 526
Gal-Yam A. et al., 2006, Nat, 444, 1053
Granot J., Sari R., 2002, ApJ, 568, 820
Hirschi R., Meynet G., Maeder A., 2005, A&A, 443, 581
Hjorth J., Bloom J. S., 2011, in Kouveliotou C., Wijers R. A. M. J., Woosley S. E., eds, Gamma-Ray Bursts. Cambridge Univ. Press, Cambridge
Houck J. C., Denicola L. A., 2000, in Manset N., Veillet C., Crabtree D., eds, ASP Conf. Ser. Vol. 216, Astronomical Data Analysis Software and Systems IX. Astron. Soc. Pac., San Francisco, p. 591
Hurley K. et al., 2007, GRB Coordinates Network, 6024
Jakobsson P. et al., 2006, A&A, 460, L13
Jarosik N. et al., 2011, ApJS, 192, 14
Jóhannesson G., Björnsson G., Gudmundsson E. H., 2006, ApJ, 647, 1238
Kalberla P. M. W., Burton W. B., Hartmann D., Arnal E. M., Bajaja E., Morras R., Pöppel W. G. L., 2005, A&A, 440, 775
Kann D. A. et al., 2010, ApJ, 720, 1513
Kann D. A. et al., 2011, ApJ, 734, 96
Laskar T., Berger E., Chary R.-R., 2011, preprint (arXiv:1102.1019)
Ledoux C., Petitjean P., Fynbo J. P. U., Møller P., Srianand R., 2006, A&A, 457, 71
Ledoux C., Vreeswijk P. M., Smette A., Fox A. J., Petitjean P., Ellison S. L., Fynbo J. P. U., Savaglio S., 2009, A&A, 506, 661
MacFadyen A. I., Woosley S. E., 1999, ApJ, 524, 262
Madau P., 1995, ApJ, 441, 18
Mészáros P., 2006, Rep. Prog. Phys., 69, 2259
Mihalas D., 1978, in Mihalas D., ed., Stellar atmospheres, 2nd edn. W. H. Freeman and Co., San Francisco, p. 650
Munari U., Zwitter T., 1997, A&A, 318, 269
Narayanan A., Charlton J. C., Misawa T., Green R. E., Kim T., 2008, ApJ, 689, 782
Panaitescu A., Kumar P., 2002, ApJ, 571, 779
Pei Y. C., 1992, ApJ, 395, 130
Perley D. A. et al., 2008, ApJ, 688, 470
Péroux C., Dessauges-Zavadsky M., D'Odorico S., Kim T.-S., McMahon R. G., 2003, MNRAS, 345, 480
Piran T., 2004, Rev. Modern Phys., 76, 1143
Poole T. S. et al., 2008, MNRAS, 383, 627
Prochaska J. X., Foley R., Tran H., Bloom J. S., Chen H., 2006, GRB Coordinates Network, 4593
Prochaska J. X., Chen H., Dessauges-Zavadsky M., Bloom J. S., 2007, ApJ, 666, 267
Prochaska J. X., Dessauges-Zavadsky M., Ramirez-Ruiz E., Chen H.-W., 2008, ApJ, 685, 344
Rauch M., 1998, ARA&A, 36, 267
Rol E. et al., 2007, ApJ, 669, 1098
Roming P. W. A. et al., 2005, Space Sci. Rev., 120, 95
Sari R., Piran T., Narayan R., 1998, ApJ, 497, L17
Savaglio S., 2006, New J. Phys., 8, 195
Savaglio S., Glazebrook K., Le Borgne D., 2009, ApJ, 691, 182
Schady P. et al., 2010, MNRAS, 401, 2773
Schady P., Savaglio S., Krühler T., Greiner J., Rau A., 2011, A&A, 525, A113
Schlegel D. J., Finkbeiner D. P., Davis M., 1998, ApJ, 500, 525

Sparre M. et al., 2011, ApJ, 735, L24

Starling R. L. C., Wijers R. A. M. J., Wiersema K., Rol E., Curran P. A., Kouveliotou C., van der Horst A. J., Heemskerk M. H. M., 2007, ApJ, 661, 787

Starling R. L. C., van der Horst A. J., Rol E., Wijers R. A. M. J., Kouveliotou C., Wiersema K., Curran P. A., Weltevrede P., 2008, ApJ, 672, 433

Thöne C. C. et al., 2011, MNRAS, 414, 479

Tiede G. P., Terndrup D. M., 1999, AJ, 118, 895

Updike A. C. et al., 2008, ApJ, 685, 361

van der Horst A. J., Rol E., Wijers R. A. M. J., Strom R., Kaper L., Kouveliotou C., 2005, ApJ, 634, 1166

van Dokkum P. G., 2001, PASP, 113, 1420

van Eerten H. J., Meliani Z., Wijers R. A. M. J., Keppens R., 2011, MNRAS, 410, 2016

Vladilo G., 1998, ApJ, 493, 583

Vreeswijk P. M. et al., 2004, A&A, 419, 927

Wainwright C., Berger E., Penprase B. E., 2007, ApJ, 657, 367

Watson D., Hjorth J., Fynbo J. P. U., Jakobsson P., Foley S., Sollerman J., Wijers R. A. M. J., 2007, ApJ, 660, L101

Woosley S. E., 1993, ApJ, 405, 273

Woosley S. E., Bloom J. S., 2006, ARA&A, 44, 507

Zafar T., Watson D., Fynbo J. P. U., Malesani D., Jakobsson P., de Ugarte Postigo A., 2011, A&A, 532, A143

Zhang B., Mészáros P., 2004, Int. J. Modern Phys. A, 19, 2385

Zoccali M. et al., 2003, A&A, 399, 931

APPENDIX A
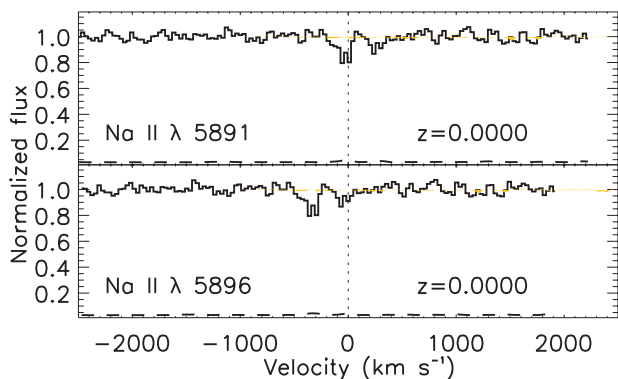
Figure A1. Galactic absorption lines detected in the FORS spectra. The error spectrum is displayed at the bottom of each panel (dashed line). The telluric features are highlighted.

Table A1. *Swift* UVOT photometry of the afterglow, corrected for Galactic extinction.

Time (d)	Brightness (mag)	Error (mag)	Filter
0.545	18.30	0.10	*v*
0.555	18.72	0.07	*b*
0.611	18.61	0.12	*v*
0.622	18.89	0.07	*b*
0.679	18.46	0.11	*v*
0.689	18.91	0.08	*b*
0.736	18.87	0.16	*v*
1.336	18.70	0.15	*uvw*1
1.340	18.69	0.17	*u*
1.349	18.90	0.11	*uvw*2
1.360	18.37	0.13	*uvm*2
1.404	19.00	0.18	*uvw*1
1.407	18.54	0.16	*u*
1.416	18.77	0.10	*uvw*2
1.427	18.76	0.16	*uvm*2
1.473	18.76	0.16	*uvw*1
1.476	18.73	0.19	*u*
1.484	19.09	0.13	*uvw*2
1.492	19.15	0.32	*uvm*2
1.743	19.03	0.25	*uvw*1
1.749	19.29	0.20	*uvw*2
1.755	19.08	0.28	*uvm*2
1.810	19.21	0.30	*uvw*1
1.816	19.12	0.18	*uvw*2
1.822	18.83	0.24	*uvm*2
1.883	19.71	0.28	*uvw*2
1.889	19.21	0.31	*uvm*2
1.944	18.71	0.21	*uvw*1
1.946	18.80	0.27	*u*
1.950	19.17	0.19	*uvw*2
1.956	19.12	0.30	*uvm*2
2.017	20.06	0.35	*uvw*2
2.084	19.42	0.22	*uvw*2
2.149	19.61	0.24	*uvw*2
2.155	19.40	0.35	*uvm*2
2.285	19.88	0.31	*uvw*2
2.348	19.16	0.36	*u*
2.421	19.53	0.25	*uvw*2
2.622	20.20	0.36	*uvw*2
2.757	20.26	0.36	*uvw*2
3.488	19.56	0.34	*uvw*1
3.502	19.53	0.34	*uvm*2

Table A2. NIR-to-X-ray SED modelling with a single power law (PL), a broken power law (BPL) and a tied broken power law (TBPL), where the spectral slopes are tied to differ by $\Delta\beta \equiv 0.5$, as expected for a synchrotron cooling break (Sari et al. 1998). Individual epochs (1.0, 1.4, 1.9, 2.5 and 2.9 d after the trigger) are modelled separately. Quoted errors refer to a 90 per cent confidence level.

Epoch	Ext. type	Model	χ^2_ν [d.o.f.]	$E(B-V)$ (mag)	$N(H)_X$ (10^{22} cm^{-2})	β_1	β_2	E_{bk} (keV)
	SMC	PL	10.71 [49]	$0.052^{+0.009}_{-0.009}$	$<7.8e{-}07$	$0.981^{+0.008}_{-0.007}$	−	−
		BPL	10.01 [47]	$0.055^{+0.008}_{-0.007}$	$<7.8e{-}07$	$0.79^{+0.04}_{-0.05}$	$1.03^{+0.01}_{-0.01}$	$0.006^{+0.001}_{-0.001}$
		TIED BPL	10.64 [48]	$0.069^{+0.008}_{-0.008}$	$<3.5e{-}06$	$\beta_2-0.5$	$1.05^{+0.01}_{-0.01}$	$0.0035^{+0.0005}_{-0.0004}$
	LMC	PL	10.29 [49]	$0.055^{+0.008}_{-0.008}$	$<7.8e{-}07$	$0.986^{+0.008}_{-0.007}$	−	−
I		BPL	9.61 [47]	$0.059^{+0.008}_{-0.007}$	$<7.8e{-}07$	$0.79^{+0.05}_{-0.05}$	$1.04^{+0.01}_{-0.01}$	$0.006^{+0.002}_{-0.001}$
		TIED BPL	10.10 [48]	$0.074^{+0.009}_{-0.008}$	$<3.2e{-}06$	$\beta_2-0.5$	$1.05^{+0.01}_{-0.01}$	$0.0031^{+0.0005}_{-0.0006}$
	MW	PL	10.16 [49]	$0.062^{+0.009}_{-0.009}$	$<7.8e{-}07$	$0.989^{+0.007}_{-0.008}$	−	−
		BPL	9.65 [47]	$0.066^{+0.008}_{-0.008}$	$<7.8e{-}07$	$0.82^{+0.04}_{-0.05}$	$1.03^{+0.01}_{-0.01}$	$0.006^{+0.002}_{-0.001}$
		TIED BPL	10.07 [48]	$0.087^{+0.008}_{-0.008}$	$<7.8e{-}07$	$\beta_2-0.5$	$1.038^{+0.008}_{-0.009}$	$0.0024^{+0.0002}_{-0.0002}$
	SMC	PL	7.62 [48]	$0.061^{+0.007}_{-0.007}$	$<9.3e{-}07$	$1.046^{+0.008}_{-0.008}$	−	−
		BPL	6.46 [46]	$0.063^{+0.007}_{-0.007}$	$<9.3e{-}07$	$1.054^{+0.008}_{-0.009}$	$-0.3^{+0.9}_{-0.4}$	$3.8^{+0.4}_{-1.7}$
		TIED BPL	7.79 [47]	$0.061^{+0.004}_{-0.004}$	$<9.3e{-}07$	$\beta_2-0.5$	$1.546^{+0.004}_{-0.004}$	$11.0^{+1.0}_{-4.6}$
	LMC	PL	40.71 [48]	$0.04^{+0.01}_{-0.01}$	$0.11^{+0.05}_{-0.05}$	$1.01^{+0.01}_{-0.01}$	−	−
II		BPL	6.15 [46]	$0.071^{+0.007}_{-0.007}$	$<9.3e{-}07$	$1.064^{+0.009}_{-0.008}$	$0.5^{+0.2}_{-1.2}$	$2.3^{+0.4}_{-0.4}$
		TIED BPL	7.53 [47]	$0.066^{+0.004}_{-0.004}$	$<9.3e{-}07$	$\beta_2-0.5$	$1.551^{+0.004}_{-0.008}$	$9.7^{+2.2}_{-3.4}$
	MW	PL	7.21 [48]	$0.091^{+0.009}_{-0.009}$	$<9.3e{-}07$	$1.059^{+0.008}_{-0.009}$	−	−
		BPL	5.87 [46]	$0.098^{+0.009}_{-0.009}$	$<9.3e{-}07$	$1.073^{+0.009}_{-0.009}$	$0.49^{+0.15}_{-1.02}$	$2.3^{+0.4}_{-0.4}$
		TIED BPL	7.36 [47]	$0.091^{+0.005}_{-0.005}$	$<9.3e{-}07$	$\beta_2-0.5$	$1.559^{+0.004}_{-0.005}$	$10.4^{+1.6}_{-4.0}$
	SMC	PL	7.62 [46]	<0.005	$0.09^{+0.07}_{-0.06}$	$1.074^{+0.009}_{-0.004}$	−	−
		BPL	7.86 [44]	<0.028	$0.13^{+0.14}_{-0.09}$	$0.9^{+0.1}_{-0.1}$	$1.12^{+0.16}_{-0.04}$	$0.006^{+0.131}_{-0.002}$
		TIED BPL	7.84 [45]	$0.027^{+0.013}_{-0.013}$	$0.26^{+0.13}_{-0.12}$	$\beta_2-0.5$	$1.25^{+0.08}_{-0.08}$	$0.015^{+0.038}_{-0.010}$
	LMC	PL	7.62 [46]	<0.007	$0.09^{+0.07}_{-0.06}$	$1.074^{+0.010}_{-0.004}$	−	−
III		BPL	7.82 [44]	<0.011	$0.08^{+0.08}_{-0.03}$	$-0.183^{+0.070}_{-0.003}$	$1.076^{+0.013}_{-0.008}$	$0.00084^{+0.00050}_{-0.00002}$
		TIED BPL	3.62 [45]	$0.03^{+0.01}_{-0.01}$	$<4.9e{-}06$	$\beta_2-0.5$	$1.19^{+0.01}_{-0.02}$	$0.00462^{+0.0010}_{-0.0008}$
	MW	PL	7.62 [46]	<0.007	$0.09^{+0.07}_{-0.06}$	$1.074^{+0.009}_{-0.004}$	−	−
		BPL	7.88 [44]	<0.026	<0.13	$0.98^{+0.08}_{-0.05}$	$1.11^{+8.e{-}08}_{-0.01}$	$0.013^{+0.005}_{-0.009}$
		TIED BPL	7.97 [45]	$0.026^{+0.019}_{-0.020}$	$0.31^{+0.13}_{-0.12}$	$\beta_2-0.5$	$1.30^{+0.08}_{-0.08}$	$0.03^{+0.08}_{-0.02}$
	SMC	PL	8.95 [48]	<0.003	$0.11^{+0.09}_{-0.08}$	$1.083^{+0.0}_{-0.003}$	−	−
		BPL	8.55 [46]	<0.023	$0.20^{+0.17}_{-0.12}$	$0.48^{+0.13}_{-0.14}$	$1.19^{+0.13}_{-0.04}$	$0.006^{+0.009}_{-0.001}$
		TIED BPL	2.05 [47]	$0.019^{+0.012}_{-0.012}$	$<2.4e{-}06$	$\beta_2-0.5$	$1.188^{+0.020}_{-0.017}$	$0.005^{+0.002}_{-0.001}$
	LMC	PL	8.95 [48]	<0.003	$0.11^{+0.09}_{-0.08}$	$1.083^{+0.0}_{-0.003}$	−	−
IV		BPL	8.48 [46]	$0.025^{+0.015}_{-0.013}$	$0.20^{+0.16}_{-0.11}$	$0.65^{+0.10}_{-0.12}$	$1.20^{+0.12}_{-0.03}$	$0.006^{+0.011}_{-0.001}$
		TIED BPL	1.99 [47]	$0.020^{+0.011}_{-0.010}$	$<2.9e{-}06$	$\beta_2-0.5$	$1.189^{+0.018}_{-0.016}$	$0.005^{+0.002}_{-0.001}$
	MW	PL	8.95 [48]	<0.003	$0.11^{+0.09}_{-0.08}$	$1.083^{+0.0}_{-0.003}$	−	−
		BPL	8.49 [46]	$0.023^{+0.013}_{-0.012}$	$0.20^{+0.16}_{-0.11}$	$0.67^{+0.10}_{-0.11}$	$1.19^{+0.12}_{-0.04}$	$0.006^{+0.012}_{-0.002}$
		TIED BPL	3.69 [47]	<0.009	$<2.2e{-}06$	$\beta_2-0.5$	$1.590^{+0.0}_{-0.006}$	$8.1^{+3.9}_{-5.5}$
	SMC	PL	7.87 [48]	<0.002	$0.10^{+0.10}_{-0.09}$	$1.062^{+0.0}_{-0.003}$	−	−
		BPL	6.73 [46]	$0.023^{+0.016}_{-0.015}$	$0.20^{+0.17}_{-0.11}$	$0.67^{+0.11}_{-0.11}$	$1.19^{+0.12}_{-0.04}$	$0.006^{+0.012}_{-0.002}$
		TIED BPL	6.69 [47]	<0.007	$0.16^{+0.10}_{-0.09}$	$\beta_2-0.5$	$1.145^{+0.0}_{-0.003}$	$0.0057^{+0.0006}_{-0.0007}$
	LMC	PL	7.87 [48]	<0.001	$0.10^{+0.10}_{-0.09}$	$1.062^{+0.0}_{-0.003}$	−	−
V		BPL	6.73 [46]	<0.0157	$0.20^{+0.17}_{-0.12}$	$0.48^{+0.13}_{-0.14}$	$1.19^{+0.13}_{-0.04}$	$0.006^{+0.009}_{-0.001}$
		TIED BPL	6.69 [47]	<0.006	$0.16^{+0.10}_{-0.09}$	$\beta_2-0.5$	$1.145^{+0.0}_{-0.003}$	$0.0057^{+0.0006}_{-0.0008}$
	MW	PL	7.87 [48]	<0.001	$0.10^{+0.10}_{-0.09}$	$1.062^{+0.0}_{-0.003}$	−	−
		BPL	6.73 [46]	<0.014	$0.20^{+0.18}_{-0.12}$	$0.49^{+0.12}_{-0.13}$	$1.18^{+0.13}_{-0.04}$	$0.006^{+0.008}_{-0.001}$
		TIED BPL	6.69 [47]	<0.005	$0.16^{+0.10}_{-0.09}$	$\beta_2-0.5$	$1.145^{+0.0}_{-0.003}$	$0.0057^{+0.0007}_{-0.0007}$

This paper has been typeset from a TeX/LaTeX file prepared by the author.